Proton-proton bremsstrahlung at 42 MeV: Measurement of cross sections and comparison with a theoretical calculation

C. A. Smith, J. V. Jovanovich, and L. G. Greeniaus*
Cyclotron Laboratory, Department of Physics, University of Manitoba, Winnipeg, Manitoba R3T 2N2, Canada
(Received 15 April 1980)

Proton-proton bremsstrahlung cross sections have been measured at 42 MeV incident beam energy using a wire chamber spectrometer developed for the study of nuclear reactions with three-body final states. Proton-proton bremsstrahlung events from a 22 cm long gaseous target were detected concurrently over polar angle ranges from 16° to 40° and all kinematically allowed values of event noncoplanarity. The data have been analyzed and compared in two different ways to a theoretical calculation based on the Hamada-Johnston potential. In a conventional analysis, the data were divided into eighteen independent polar angle regions and the $d^3\sigma/d\Omega_1 d\Omega_2 d\psi_\gamma$, $d^2\sigma/d\Omega_1 d\Omega_2$, and $d^2\sigma/d\theta_1 d\theta_2$ cross sections were determined and compared with the theoretical calculations. In a "global" analysis, the data were compared directly with a theoretically weighted, simulated set of events. The latter comparison was made in terms of a wide range of variables, both in the laboratory and in the center of mass systems. A significant discrepancy between experiment and theory was found in certain parts of the observed phase space.

[NUCLEAR REACTIONS Bremsstrahlung $p(p,p\gamma)p$, $E=42.0$ MeV; measured $d^3\sigma/d\Omega_1 d\Omega_2 d\psi_\gamma$, $d^2\sigma/d\Omega_1 d\Omega_2$, $d^2\sigma/d\theta_1 d\theta_2$; global analysis; compared calculations Hamada-Johnston potential.]

I. INTRODUCTION

A. Reasons for studying the *pp* bremsstrahlung process

Proper understanding of the nucleon-nucleon interaction is important because it has many applications in diverse areas of nuclear physics. The known properties of the nuclear force have been summarized in the form of several phenomenological nucleon-nucleon potential models. With simplicity being the guiding principle, these potentials incorporate only those terms allowed by the known conservation laws which are necessary to describe the existing experimental data.[1,2]

Until the present, the only data available for the determination of the potential parameters were obtained from *pp* and *np* elastic scattering experiments. Of necessity then, only information on the elastic or on-energy-shell (ONES) nature of the *NN* interaction has been built into the detailed specification of the potential models. However, all nuclear processes other than *NN* elastic scattering depend, to some degree, on the off-energy-shell (OFES) portions of the *NN* interaction. Some applications of potential models to the OFES phenomena have not yet yielded satisfactory results.[3] Nuclear structure calculations are very complex and it is not clear whether the inability to reproduce the experimental results is due to the approximations made in these calculations or because the potential models used do not represent the OFES interaction adequately. Therefore, it is very important that the OFES behavior of the *NN* force be understood first in elementary reactions.

Elastic scattering experiments cannot reveal anything about the OFES properties of the *NN* interaction and cannot, even in principle, distinguish between phase equivalent potentials such as the Hamada-Johnston potential and the nonlocal, momentum-dependent potentials derived from it by applying certain unitary transformations.[3] In order to learn something about the *NN* interaction OFES, it is necessary to study inelastic processes where the OFES effects are both experimentally observable and unambiguously calculable theoretically.

NN bremsstrahlung is the simplest and most direct process that can be used for this purpose because there are only two strongly interacting particles involved in the interaction. Any other inelastic process, such as pion production or nucleon-deuteron scattering, involves three or more strongly interacting particles, which greatly complicates the theoretical analysis.

The information which the bremsstrahlung process can be expected to provide may be summarized in the form of two, still unanswered, questions:

(1) Is the long range part of the current potential models "good" OFES? Most of the potential models are similar to each other at large distances. Although the long range part of the potentials describes the ONES part of the *NN* interaction very well, it has never been tested OFES. Therefore, it is important to find out if this "well known" part of the potential is good OFES.

(2) If the answer to question (1) is positive, we must then ask: Which of the potential models gives the best description of the nucleon-nucleon

force at short distances where most of the potentials differ substantially from each other?

Heller[4] and Bohannon[5] have investigated the effects of various unitary transformations on the *pp* bremsstrahlung (ppB) cross sections and have found effects of differing magnitudes at both relatively low (around 40 MeV) and relatively high (150–200 MeV) energies. In general, the effects at higher energies are larger than at lower energies but, even at relatively small energies, the effects may be experimentally observable. At low energies, one is testing preferentially the OFES effects due to the long range part of the *NN* potential while at high energies, effects due to both the long and short range parts should appear. Therefore, it is of interest to study the bremsstrahlung reaction at *both* high and low energies. Due to the relatively low incident energy, the experiment reported in this paper is expected to yield information about the long range part of the *NN* force.

The initial interest in studying the ppB process was generated in 1963 when Sobel and Cromer[6] evaluated the ppB cross section in a distorted-wave Born approximation (DWBA) approximation using the Hamada-Johnston (H-J) potential. Since the first ppB experiment was performed at Harvard,[7] about two dozen experiments have been performed, most of them with rather low accuracy. A review of all of the experiments performed by the summer of 1977 is contained in articles by Halbert[8] and Jovanovich.[9]

B. Summary of the experiment

The experiment described in this paper represents a major departure, both in experimental technology and in its analysis procedures, from earlier bremsstrahlung experiments. In all previous experiments, except for the one performed at Rochester,[10] the scintillation counter technology common in low energy nuclear physics was used. As a result, all of those experiments were characterized by small solid angles, relatively poor angular resolution, and counting rates of only a few ppB events per hour. In the work reported here, high energy wire chamber technology and extensive on-line and off-line computer analysis on an event-by-event basis were applied for the first time to a low energy experiment. The benefits of using this technology were a 100-fold increase in data taking rates and a five-fold improvement in the angular resolution when compared to previous ppB experiments performed at similar energies.

The experiment reported here was performed in two parts, henceforth referred to as Exp. I and Exp. II. Some major results and conclusions from these experiments have been previously reported in three short letters,[11-13] henceforth referred to as L1, L2, and L3, and in a review paper.[9] In Exp. I, only a few thousand events were collected, yielding statistical errors comparable to the estimated systematic errors. In Exp. II, certain improvements were made in both the experimental apparatus and the analysis procedures, and more events were collected. The data from Exp. II were processed twice; the results of the "first analysis" allowed us to identify particular problems. Some refinements in the analysis were then incorporated in a "reanalysis." A summary of some of the characteristics of the two experiments is given in Table I. The apparatus has been described previously in detail in a series of five papers,[14-18] henceforth referred to as P1–P5. Additional details of the apparatus and analysis procedures can be found in four theses,[19-22] henceforth referred to as T1–T4, and the Supplement,[23] henceforth referred to as S or by the section number as used in the Supplement.

The wire chamber spectrometer shown in Fig. 1 was used in the experiment for the detection of the ppB events. The energies and the angles of both final state protons were measured. Using the four energy-momentum conservation relations, the photon energy and angles, and a goodness-of-fit parameter were calculated. The ppB cross sections were determined relative to the *pp* elastic cross section by detecting *pp* elastic events concurrently with the ppB data in the same apparatus.

The spectrometer consisted of a scattering chamber and two arms located on either side of the incident beam (also see P1, T1, and T4). Each arm contained two wire chambers and a large 22.5 cm×22.5 cm plastic scintillation counter, which were used to measure the angles and energies of the outgoing protons. This enabled the complete range of kinematically allowed event noncoplanarities for the large domain of polar angles delimited by the heavy outside rectangle in Fig. 2 to be detected concurrently.

Coincidences between signals from the scintillation counters S_L and S_R (cf. Sec. 3.6 in P1) provided a trigger if the pulse heights corresponded to protons with energies in the ppB kinematic region. Random events were also recorded by triggering on coincidences with the signal from S_R delayed by one cyclotron rf period. The counter pulse height information and the spark positions recorded in a ferrite core memory were read into a PDP-15 computer (cf. P2). The coordinate data from the wire chambers were later used to improve the effective resolution of the counters by correcting for the spatial nonuniformities in the

TABLE I. Summary of experiments.

	Exp. I	Exp. II	
		First analysis	Reanalysis
Detected energy threshold	7.5 MeV	4.5 MeV	4.5 MeV
Scattered energy threshold	10 MeV	7.0 MeV	7.0 MeV
Number of ppB event candidates	5343	10449	8402
Number of random events	634	847	435
Number of prompt background events [a]	223	1022	772
Number of ppB events used in conventional analysis [b]	2049	8576	7195
Number of ppB events used in global analysis			7190

[a] The percentage of prompt background events is larger in Exp. II because such events occur preferentially with small energies for at least one of the protons.

[b] Because of systematic effects, the number of events used in the conventional analysis is less than the number of net (i.e., all background subtracted) ppB event candidates. This is especially true in the case of Exp. I.

counter pulse height response (cf. P5 and T2).

A beam positioning device (cf. P5 and T2) was used to stabilize the centroid of the beam to a fraction of a millimeter with respect to the center line of the scattering chamber. A long gaseous hydrogen target[24] was used, which allowed a large fraction of the random background to be eliminated by means of vertex rejection criteria. The down-

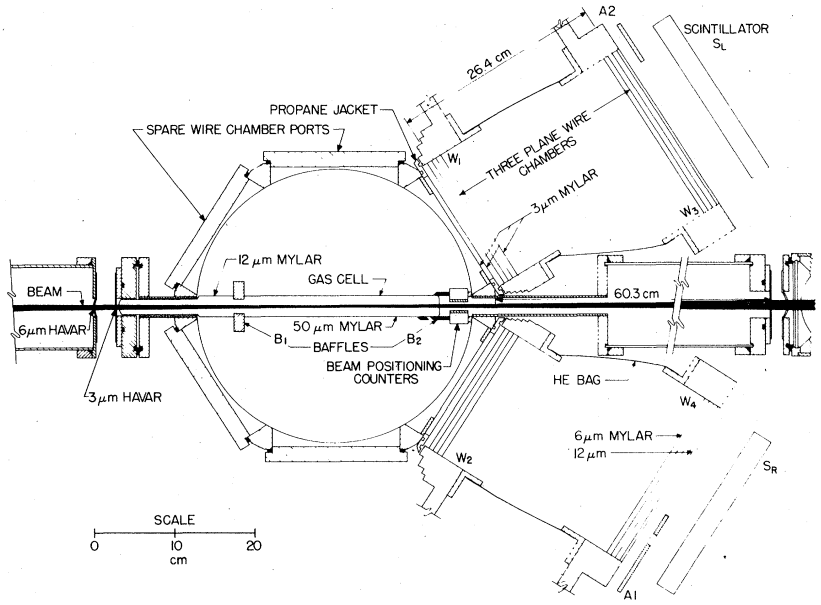

FIG. 1. A scale drawing of the spectrometer showing the scattering chamber, the wire chambers ($W1$ to $W4$), the scintillation counters (S_L and S_R), and the beam entrance and exit ports. Each wire chamber contained three coordinate planes with wires oriented horizontally, diagonally, and vertically. The upstream baffles $B1$ prevented protons which were multiple-scattered in the entrance HAVAR foils from entering the wire chambers. Plastic bags containing He gas were used between the front and rear wire chambers to reduce energy loss and multiple scattering.

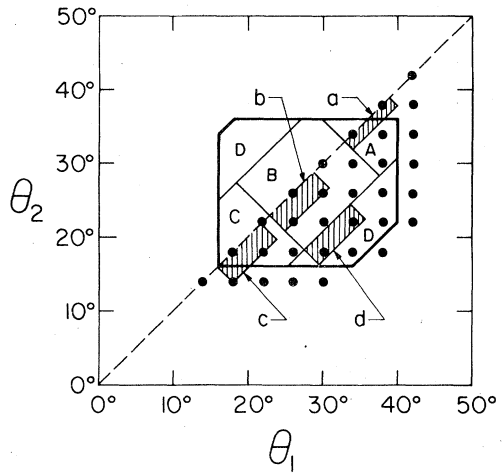

FIG. 2. A schematic representation of the proton polar angles of interest in this experiment. The outside rectangle outlines the ranges of polar angles covered by the equipment used. The full dots represent the θ_1-θ_2 proton angle pairs at which numerical computations of the ppB cross sections were made. The areas A, B, C, and D represent the areas over which the data was integrated in the experiment to theory comparison outlined in Figs. 24 and 25. The shaded rectangles labeled a, b, c, and d represent the areas of the θ_1-θ_2 plane over which the cross sections and squares of matrix elements presented in Figs. 27 and 28, respectively, were averaged.

stream baffles $B2$, and the baffles $A1$ and $A2$ behind the rear wire chambers, were designed to allow detection of some pp elastic events with 44.7° polar angles (cf. T4). These events were used for the cross section normalization and for control of gain drifts in the photomultiplier tubes.

The recording of the spark and proton energy information, initial data reduction, track reconstruction, and vertex determination were performed on-line by a PDP-15 computer (cf. P3). Events accepted by the PDP-15 were sent on-line to a 360/65 computer via a high speed data link, which then performed a more complete kinematic and statistical analysis, recorded the data on magnetic tape, and provided on-line feedback of the fully analyzed events (cf. P3 and Sec. S II).

Most of the general properties of the spectrometer have been reported in P1. Since that time, further extensive investigations of various aspects of the experimental apparatus have been made, both by direct measurement and by a Monte Carlo simulation. Because of their specialized nature, the discussion of these properties is contained in S and a summary of all the important spectrometer properties is presented in Table II.

An extensive comparison of the experimental results with a particular Hamada-Johnston potential model calculation was made. Two separate analysis and comparison techniques were used. In the first method, the experimental cross sections were obtained in a "conventional" manner but all corrections due to the detection efficiency and resolution of the apparatus were accounted for by Monte Carlo techniques. The principal results of this analysis were reported in L1 and L2. In the second analysis, which was quite different from the analysis procedures commonly used in low energy nuclear physics, an extensive comparison of the experimental results with the theoretical calculation was made in an unconventional way. This method of analysis which, for convenience, we call the "global" analysis, was based entirely on Monte Carlo simulation procedures and the principal results were reported in L3 and Ref. 9.

II. DATA ANALYSIS METHODS

Certain aspects of the experiment reported here were quite different from those encountered in a typical low energy ($\lesssim$150 MeV) experiment. Because of this, the determination of the experimental cross sections required developing certain procedures which have not been used in other low energy experiments. This section explains the basic method used to analyze the data and to make the comparison between experiment and theory.

A. Relationship between the cross sections and experimental distributions

In general, the variables measured in a given experiment do not correspond directly to those which a theorist would calculate. Experimental factors, such as multiple scattering, energy loss, finite sized detectors, etc., cause the observed variables to differ from the theoretical ones. Because of this, it is convenient to distinguish between the experimentally determined value of a given quantity and the value of the same quantity at the point where the interaction occurs. The former will be referred to as the "experimental" (if determined from the experimental data) or "randomized" (if determined from the simulated data) value, while the latter will be referred to as the "theoretical" or "nonrandomized" value of the quantity in question. The vector $\vec{q}$ is used to denote the set of experimental variables [e.g., $\vec{q} = (\theta_1, \theta_2, \phi_r, \psi_r)$], which describe the observed distributions, while the vector $\vec{q}'$ will be used to denote the corresponding set of theoretical variables [i.e., $\vec{q}' = (\theta_1', \theta_2', \phi_r', \psi_r')$]. These two sets of quantities are related through a response function $K'(\vec{q}', \vec{r}'; \vec{q}, \vec{r}, \vec{s})$ which gives a complete description of the properties of the detection system. The vectors $\vec{r}$ and $\vec{s}$ are used to denote the remaining measured or

TABLE II. Spectrometer properties. All resolutions expressed as FWHM (Ref. 25).

Geometrical		
Maximum polar angle range		14°–48°
Maximum azimuthal angle range		±38°
Solid angles subtended by spectrometer	(left)	0.22 sr
arms at center of scattering chamber	(right)	0.16 sr
Measurement of energies (MeV)		
Low energy cutoff in detected	(left)	4.4 MeV
proton energies	(right)	4.6 MeV
Detected proton energy resolution		$0.42/E^{1/2}$
Missing particle energy resolution		$0.60/(E_0-E_m)^{1/2}$
Measured resolutions		
For 21 MeV protons at θ =44.7°		1.04°
For 12 MeV protons at θ =44.7°		1.60°
Normalized vertical vertex error		0.28 cm
Normalized horizontal vertex error		0.58 cm
Resolutions from the simulated data—average over all ppB events detected by the spectrometer		
Proton polar angles θ_L and θ_R		1.7°
Relative noncoplanarity ϕ_r		0.44
Photon angle ψ_γ		44°
Lab photon energy relative to kinematic maximum		9.4%
c.m. photon energy relative to kinematic maximum		4.0%
Proton polar angles in c.m. θ_p^*		7°
c.m. angle δ^*		30°
c.m. angle β^*		30°
Miscellaneous		
Vertex rejection factor for gaseous H_2 target		≈95%
Maximum data-taking rate		75 events/sec
PDP-15 processing time/good event		≈15 ms
IBM 360/65 processing time/good event		≈15 ms

inferred variables needed to complete the description of the experimental system. Two sets are used in order to distinguish between the vertex coordinates, for which it is meaningful to define a theoretical equivalent ($\vec{r}'$), and those variables (e.g., spark coordinates, vertex errors, χ^2, etc.) for which such a definition is meaningless.

The probability of an event originating with variables $\vec{q}'$ and $\vec{r}'$ being detected in the ranges $d\vec{q}$, $d\vec{r}$, and $d\vec{s}$ is given by

$$K'(\vec{q}',\vec{r}';\vec{q},\vec{r},\vec{s})d\vec{q}\,d\vec{r}\,d\vec{s}\,. \tag{1}$$

If $\vec{q}'$ and $\vec{r}'$ are uniformly distributed within the ranges $\Delta\vec{q}'$ and $\Delta\vec{r}'$, then the probability of an event originating with $\vec{q}'$ and $\vec{r}'$ within these ranges being detected by the spectrometer in the range $\Delta\vec{q}$ centered at $\vec{q}_0$ is given by

$$\int_{\Delta\vec{q}} d\vec{q} \int_{\Delta\vec{q}'} d\vec{q}' \int_{\Delta\vec{r}'} d\vec{r}' \iint_{\text{spec}} K(\vec{q}',\vec{r}';\vec{q},\vec{r},\vec{s})d\vec{r}\,d\vec{s}\,, \tag{2}$$

where "spec" designates that the integrations over $d\vec{r}$ and $d\vec{s}$ are taken over the ranges allowed by the spectrometer. The number of ppB events detected by the spectrometer within the range $\Delta\vec{q}$ can then be written

$$\Delta N^{\text{ppB}}(\vec{q}_0) = RlI(\vec{q}_0)\,\Delta\vec{q}\,, \tag{3}$$

where

$$I(\vec{q}_0) = \frac{1}{\Delta\vec{q}} \int_{\Delta\vec{q}} d\vec{q} \int_{\text{all}} d\vec{r}' \int_{\text{all}} d\vec{q}' \times \iint_{\text{spec}} K(\vec{q}',\vec{r}';\vec{q},\vec{r},\vec{s})\,\frac{d\sigma(\vec{q}')}{d\vec{q}'}\,d\vec{r}\,d\vec{s}\,. \tag{4}$$

The range of integration over $\vec{r}'$ and $\vec{q}'$ is taken sufficiently large so that K vanishes outside the limits. The quantity $d\sigma(\vec{q}')/d\vec{q}'$ is the appropriate ppB cross section and l is the nominal target length. R is an overall normalization constant equal to

$$R = \int \epsilon_s(t)n(t)I(t)[1-D(t)]dt\,. \tag{5}$$

This integration is performed over the entire data collection time of the experiment. The quantities $\epsilon_s(t)$, $n(t)$, $I(t)$, and $D(t)$ represent the efficiency of the system in recognizing and unambiguously reconstructing an event, the number of hydrogen

atoms per unit volume, the number of incident protons per unit time, and the dead time of the system, respectively. The method used to evaluate R is discussed in Sec. VII.

B. Experiment to theory comparison

Two different methods were used to compare the experimental data with the theoretical calculations. A diagram depicting the major steps in the conventional and global methods is shown in Fig. 3. The Hamada-Johnston potential was used to calculate a large table of ppB cross sections (see Sec. III) which was used as input for the Monte Carlo simulation program. This program, which is described in Sec. IV, produced a set of $\sim 10^5$ events which were weighted according to the ppB cross sections and which reproduced all important experimental effects. These events were then used to form a series of histograms. It is in the use of these histograms that the conventional and global methods diverge.

In the conventional analysis, the cross sections were determined from the experimental histograms by solving Eq. (3) for $d\sigma(\vec{q}')/d\vec{q}'$ (see Sec. VIII A for details). These cross sections were then compared directly with the calculated cross sections as shown by a double arrow in Fig. 3. The problem with this method was that it was necessary to introduce certain approximations and corrections in the solution of Eq. (3). The only practical way to do this was to use the histograms of the simulated data. This is indicated by the arrow labeled "correction" in Fig. 3. This procedure makes the results dependent on the theory to be tested.[26] While this is in principle unsatisfactory, in practice it is often an adequate analysis method.

The global method avoids this problem completely because the experimental cross sections are never computed. The experiment to theory comparison is made directly between the simulated histograms and similar ones formed from the experimental data. This is again shown by a double arrow in Fig. 3. In addition, the global method has the following advantages over the conventional method. First, integration over all variables not under investigation can be performed easily, allowing the experiment to theory comparison to be made at the level of single differential cross sections. As a result, relatively high statistics per bin can be achieved, allowing more accurate tests of particular aspects of the theory. Second, the global method allows an easy change of variables and the comparison of experiment to theory can be made easily in terms of any desired variable. In fact, this procedure can be used to determine those variables and regions of phase space which provide the most sensitive test of theory. As shown in Sec. SIV, this procedure also proved to be valuable in studying various properties of the experimental system and in the detailed investigation of systematic errors.

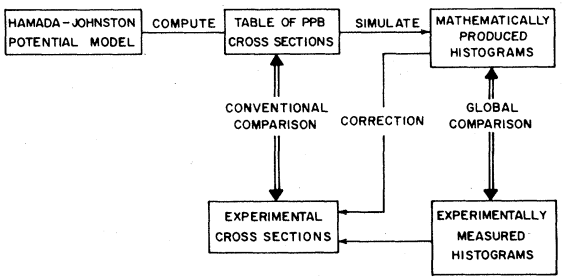

FIG. 3. A schematic representation of the major steps used in the conventional and global analysis procedures.

III. THEORETICAL CROSS SECTIONS

A. Method

The ppB cross sections were calculated according to the method originally developed by Liou and Cho.[27] The calculations were performed in the laboratory system using the Hamada-Johnston hard-core potential. The nuclear interaction was treated exactly and the electromagnetic interaction in the Born approximation. Relativistic spin corrections were included in the electromagnetic Hamiltonian, but Coulomb effects and exchange terms were neglected. In a later publication by Liou and Sobel,[28] the results of this calculation were compared with a similar calculation done in the center-of-mass system. As is shown in Figs. 2, 4, 9, and 12 of Ref. 28, the maximum discrepancy between the codes is about 10% for the $d^3\sigma/d\bar{\Omega}_1 d\bar{\Omega}_2 d\psi_\gamma$ cross sections. For the integrated cross sections, the discrepancy would be smaller.

The Harvard coordinate system described in Appendix A was used in the calculation and the $d^3\sigma/d\bar{\Omega}_1 d\bar{\Omega}_2 d\psi_\gamma$ differential cross sections were computed. The calculated cross sections spanned the full range observed in the spectrometer with 4° spacing in the scattering angles of the protons. For each $\bar{\theta}_1$-$\bar{\theta}_2$ combination, the cross sections were evaluated at 10° intervals in ψ_γ for five values of the noncoplanarity. The $d^2\sigma/d\bar{\Omega}_1 d\bar{\Omega}_2$ and $d^2\sigma/d\bar{\theta}_1 d\bar{\theta}_2$ cross sections were obtained by integrations over ψ_γ and ϕ_1 and ϕ_2, respectively. Their exact definitions are given in Appendix B.

B. Results

In Figs. 4 and 5, some representative cases of the $d^3\sigma/d\bar{\Omega}_1 d\bar{\Omega}_2 d\psi_\gamma$ and $d^2\sigma/d\bar{\Omega}_1 d\bar{\Omega}_2$ cross sections are given. In Fig. 6 and Table III, the $d^2\sigma/d\bar{\theta}_1 d\bar{\theta}_2$ cross sections are plotted and listed. The numer-

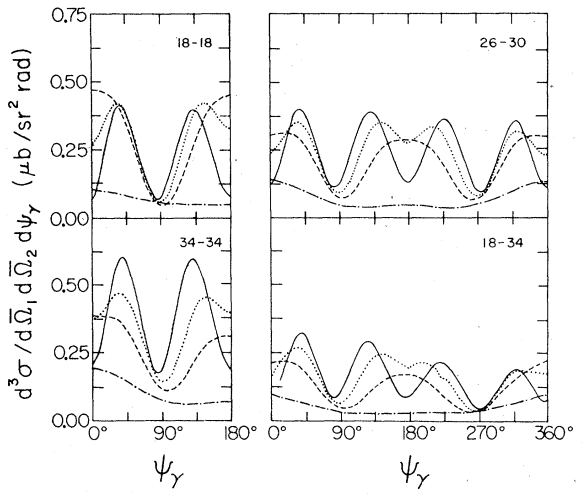

FIG. 4. The computed differential cross sections $d^3\sigma/d\bar{\Omega}_1 d\bar{\Omega}_2 d\psi_\gamma$ are shown as a function of the photon angle ψ_γ for four different values of the relative noncoplanarity at the polar angle pairs indicated on the drawings. The ordering of the curves is such that the solid, dotted, dashed, and dot-dashed curves correspond to the points labeled 1, 3, 4, and 5 in Fig. 5, respectively. A fifth curve (corresponding to the point 2 in Fig. 5) has been omitted to avoid overcrowding. The calculations were made in 10° intervals in ψ_γ and the curves shown represent a smooth interpolation of these calculations.

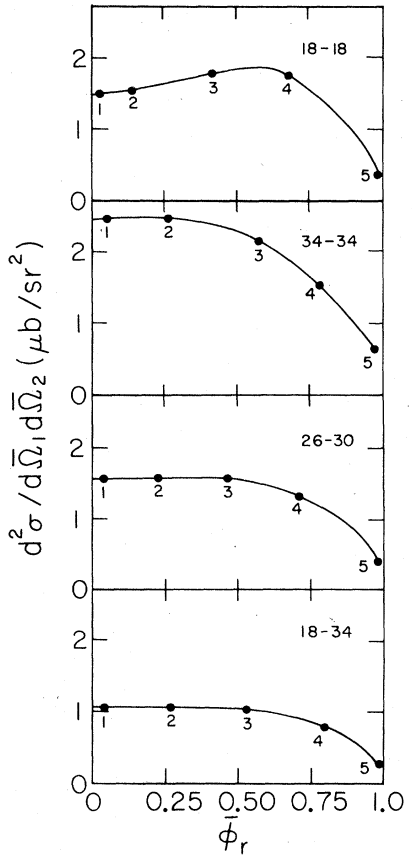

FIG. 5. The computed cross sections $d^2\sigma/d\bar{\Omega}_1 d\bar{\Omega}_2$ are presented as a function of the relative noncoplanarity ϕ_r for several characteristic pairs of proton polar angles. The solid lines serve only to guide the eye.

ical values of all computed cross sections are given in Sec. S VI.

Due to the numerical approximations used in these calculations, small discontinuities appear in the data at $\psi_\gamma = 0°$ and $\psi_\gamma = 180°$ for some cases of noncoplanar and asymmetric angles. In fact, the cross sections were calculated at $\psi_\gamma = 1°$ and $359°$ and $\psi_\gamma = 179°$ and $181°$ rather than $\psi_\gamma = 0°$ and $180°$ to avoid numerical difficulties. As these discontinuities in the cross sections are small, they are considered to be of no consequence for the results reported in this paper.

IV. DATA SIMULATION

A. Event generation

The first step in the simulation procedure was to generate an event at random in the center-of-mass system. This consisted of selecting the momentum components of three final state particles constrained only by the kinematics of the reaction. A modified version of the random star generator contained in the program OWL[29] was used to accomplish this. The event was then transformed to the laboratory system and a vertex was chosen at random within the reaction volume of the target. Following this, each proton was traced through the spectrometer. The effects of multiple scattering and energy loss were calculated, the spark coordinates generated, and the randomized detected energies determined. The event was then reconstructed by processing it through the same routines which were used to reconstruct an experimental event.

For practical reasons, the following approximations were introduced into the simulation procedure:

(1) The vertical beam profile was assumed to be Gaussian and the event distribution along the beam direction to be uniform (see Sec. S IV C).

(2) Multiple scattering was approximated by a Gaussian distribution instead of a Molière distribution.[30]

(3) The energy loss calculations were based on an interpolation from tabulated values. The results were checked against tables[31] and agreement to better than 1% was found.

(4) Straggling effects in the energy loss were ignored because the spread of detected proton energies in the scintillation counters was dominated

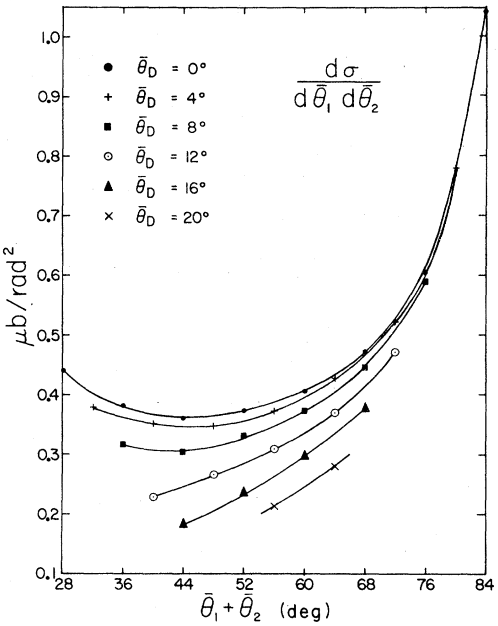

FIG. 6. The calculated cross sections $d^2\sigma/d\bar{\theta}_1 d\bar{\theta}_2$ are shown as a function of the sum of the proton polar angles, $\theta_S = \theta_1 + \theta_2$, for different asymmetries, $\theta_D = |\theta_1 - \theta_2|$. The solid lines are to guide the eye only.

by the energy resolution of counters.

(5) The resolution in the detected energy was approximated by $\delta E/E \sim 0.42/\sqrt{E}$ (cf. P3 and T4).

(6) The nuclear reaction tails in the scintillator response function were smaller[32] than 1%; thus they were ignored.

(7) The dependence of the pulse height response of the scintillators on the proton position was not included.

(8) Neither the high nor the low discriminator cutoffs were randomized. Both this and the preceding effect were compensated for by careful selection of the energy cuts applied to the simulated data (see Sec. SIV A).

(9) The screening effects of the baffles $B1$ and $B2$ were not simulated. This was compensated for by restricting the effective target length (see Sec. SIV C).

(10) No attempt was made to simulate missing sparks or double tracks and the existence of the diagonal coordinates was ignored. In both the conventional and global analysis, the normalization procedures compensated for their effects. Problems could only arise if such inefficiencies were localized in one region of the spectrometer (see Sec. SIV B).

(11) The pp elastic (normalization) events were not simulated.

(12) No allowance was made for skewness, divergence, or lateral displacement of the incident beam (see Sec. SIV C).

TABLE III. Theoretical $d^2\sigma/d\bar{\theta}_1 d\bar{\theta}_2$ cross sections.

$\bar{\theta}_1, \bar{\theta}_2$ (deg)	$d^2\sigma/d\bar{\theta}_1 d\bar{\theta}_2$ (μb/sr^2)	$\bar{\theta}_1, \bar{\theta}_2$ (deg)	$d^2\sigma/d\theta_1 d\theta_2$ (μb/sr^2)
18-18	0.382	22-30	0.331
22-22	0.361	26-34	0.373
26-26	0.374	30-38	0.445
30-30	0.406	34-42	0.589
34-34	0.472	14-26	0.229
38-38	0.605	18-30	0.265
14-18	0.379	22-34	0.309
18-22	0.350	26-38	0.368
22-26	0.348	30-42	0.478
26-30	0.373	14-30	0.184
30-34	0.426	18-34	0.237
34-38	0.522	22-38	0.298
38-42	0.779	26-42	0.378
14-22	0.317	18-38	0.213
18-26	0.340	22-42	0.279

B. Determination of weights

Since the objective of the experiment was to compare the measured data with a theoretical calculation, the final step in the generation of each simulated event was to calculate its theoretical weight (cf. T4 for details). In brief, the weights W were defined as follows:

$$\frac{d^3\sigma}{d\Omega_1 d\Omega_2 d\psi_\gamma} = WR_3 = \frac{\alpha E_1' E_2'}{\pi^2 m^3 p_0} < \tfrac{1}{4}\,\mathrm{tr} M^\dagger M > R_3 , \quad (6)$$

where R_3 is the three body Lorentz-invariant phase space factor, $\sqrt{\alpha}$ and m are the proton charge and mass, respectively, p_0 is the incident proton laboratory momentum, E_1' and E_2' are the proton energies in the final state, and M is the matrix element computed on the basis of a specific theoretical model.

Since the kinematic parameters for the simulated ppB events were chosen at random, they seldom coincided with points for which the matrix elements were evaluated. As a result it was necessary to interpolate between different matrix elements to obtain the proper weight for each event. This was done using the subroutine SPLINEFIT [33] which made a two dimensional interpolation of the weights on the ψ_γ-ϕ_γ surface and a simple two-way linear interpolation on the θ_1-θ_2 surface. This interpolation procedure was tested for a number of randomly selected events by comparing the interpolated weights with weights computed at the same points using Liou's cross section program.[27] The differences observed were always smaller than a few percent.

C. Detection efficiency and acceptance

Using the simulated data, the spectrometer efficiency and geometrical acceptance were studied. In Fig. 7, scatter plots of the detected events (without energy cuts) are shown for each of the spectrometer arms. The top half of the figure shows the relationship between the vertex position Z and the proton polar angles θ, while the correlations between the azimuthal angle ϕ and the polar angles are given in the bottom half.

Figure 8 illustrates the fraction of phase space observed in the experiment. In the top half of the figure, scatter plots of all (the simulated) events are presented, while in the bottom half, only those events detected by the spectrometer are shown. The plot of the c.m. photon energy k^* versus the sum of the proton polar angles, $\theta_S = \theta_1 = \theta_2$, illustrates the correlation between these variables. A comparison of parts (a) and (c) shows that the range of photon energies detected in this experiment was very favorable for the detection of OFES effects.

V. ENERGY CALIBRATION AND ANGULAR RESOLUTION

The basic properties of the spectrometer have been discussed in P1. Further details are given in Sec. S III. A summary of the most important properties is presented in Table II. In this section, the energy calibration of the scintillation counters and the determination of the angular resolutions are discussed in detail, as they are important for the interpretation of the results.

A. Energy calibration of the scintillation counters

In Exp. I, the photomultiplier voltages were chosen in order to obtain a linear pulse height energy relationship for proton energies up to about 37 MeV. This procedure resulted in detected proton energy thresholds of 7.5 MeV. In that experiment, the scintillators were calibrated by observing pp elastic events at 45° at a number of incident beam energies ranging from 42 down to 23 MeV, which was the minimum energy available from the cyclotron.

In Exp. II, the photomultiplier voltages were raised, causing the response curves to become somewhat nonlinear above ~20 MeV, and the differential discriminator cutoffs were lowered. This resulted in the energy thresholds being lowered to ~4.5 MeV (detected energy) and allowed significantly more data to be obtained at the smallest and most asymmetric polar angles. The calibration curves for the two counters were obtained by triggering the spectrometer on random coincidences produced by protons elastically scattered

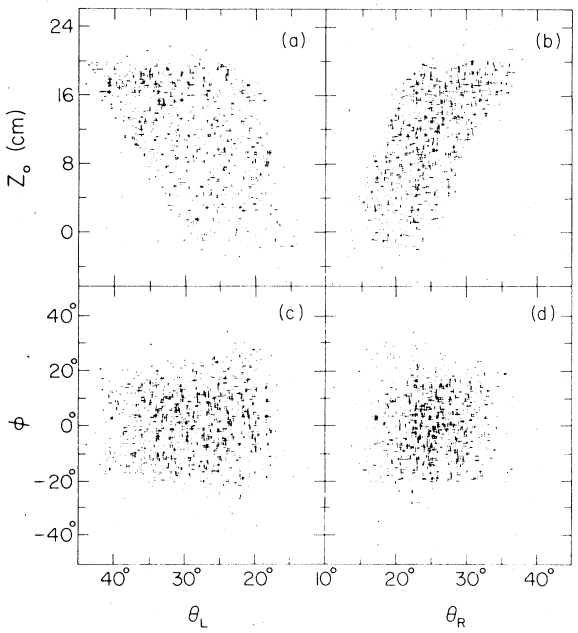

FIG. 7. Scatter plots of the simulated ppB events geometrically detected (no energy cuts applied) by the spectrometer are shown, illustrating the dependence of the geometrical acceptance on the vertex position Z_0, proton polar angle θ, and azimuthal angle ϕ.

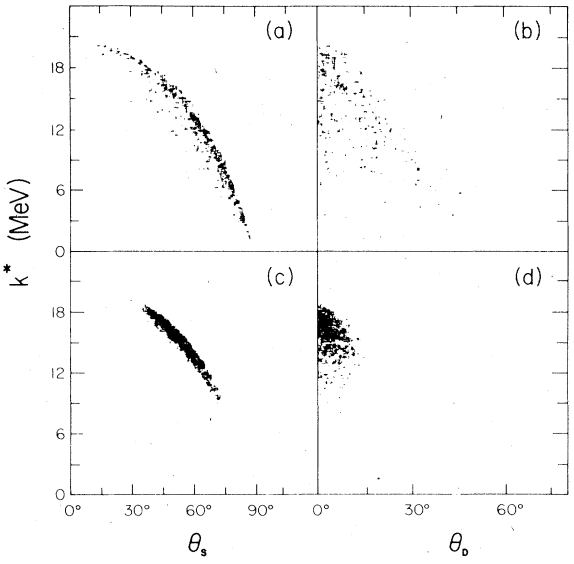

FIG. 8. Scatter plots of the simulated ppB events are shown, depicting the acceptance range of the spectrometer in terms of k^*, θ_S, and θ_D. In parts (a) and (b), a sample of ~1000 generated events is shown. In parts (c) and (d), an equal sample of events detected by the spectrometer is shown.

within the full fiducial volume of the H_2 gas target and detected over the entire surface of the scintillation counters. Three different beam energies, 42.2, 31.5, and 23.0 MeV, were used. The results are shown in Fig. 9. The lines labeled *LA* (*RA*) and *LB* (*RB*) were obtained by fitting the data in the energy range between 10 and 25 MeV with a linear (quadratic) function. As no calibration points existed below 10 MeV, it was assumed in L2 that the curves *LA* and *RA* adequately describe the pulse height energy relationship in this energy range. This extrapolation is considered to be the weakest part of the experiment,[34] so further studies were performed (see Sec. SIV A). The dashed lines *LB* and *RB* in Fig. 9 are alternate calibration curves which were also consistent with the data. The curves deemed to be the best, and used for all global results presented in this paper, consisted of the *LA/RB* combination. The results obtained using the *LA/RA* and *LB/RA* combination were taken to be a measure of the uncertainty associated with the calibration procedure.

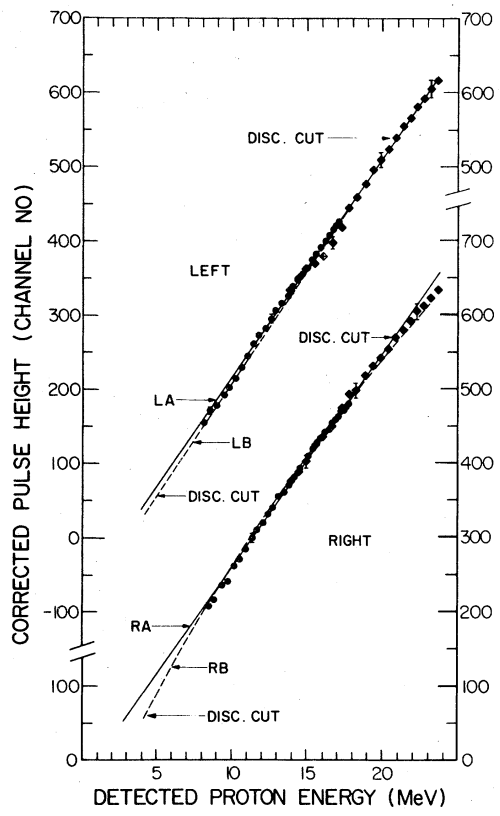

FIG. 9. The pulse height energy calibration for both the left and right scintillation counters for Exp. II. The crosses indicate the data taken at 31.5 MeV and the dots the data at 23.0 MeV. The 42.2 MeV data are not included as they lie primarily above the energy region shown. The errors quoted with several of the points are estimated and come mainly from the uncertainty in the pulse height response matrix. The arrows indicate the position of the fast discriminator cutoffs. The significance of the solid (*LA* and *RA*) and dashed (*LB* and *RB*) curves is discussed in the text.

B. Angular resolution

The angular resolutions[25] for the outgoing protons depended on their angles and energies. Since it was impractical to measure the resolutions for a large variety of experimental conditions, the following procedure was used (cf. Sec. 5.8 of P1 and Appendix C of T4 for details). First, the polar and azimuthal angle resolutions were determined by measuring the sum θ_S of the polar angles and the difference ϕ_D of the azimuthal angles for elastically scattered protons at 44.7° at 42 and 24 MeV incident proton energies. Then, these results were extrapolated to other angles and energies observed in the experiment by calculating the contributions from the wire spacing in the wire chambers and multiple scattering in the spectrometer as a function of the proton angles and energies (see Sec. 5.8 in P1 and Sec. 4.3a in T4). The results of these measurements and calculations are shown in Fig. 10. They were also compared with angular resolutions computed using a simulated sample of ppB events (see Sec. SV A for details).

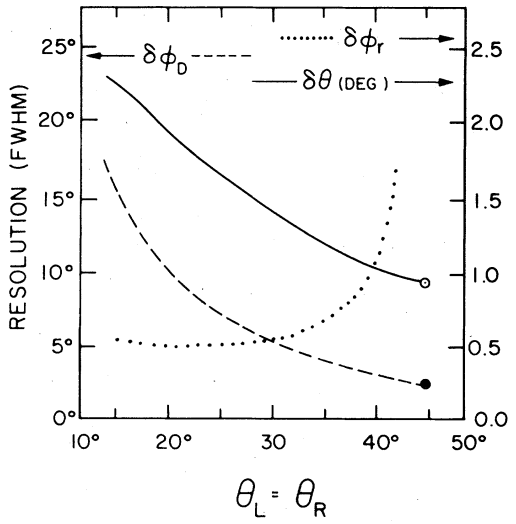

FIG. 10. The computed resolutions (Ref. 25) (FWHM) in proton polar angle ($\delta\theta$), azimuthal event noncoplanarity ($\delta\phi_D$), and relative noncoplanarity ($\delta\phi_r = \delta\phi_D/\phi_{DM}$) for symmetric ppB events at 42 MeV are shown as full, dashed, and dotted lines, respectively. Note that different scales are used for the different curves. The points shown at 45° were determined from the measurements of θ_S and ϕ_D on *pp* elastic events (cf. Sec. 5.8 in P1).

VI. ppB EVENT SELECTION

The off-line event selection consisted of two basic steps. First, the individual events were subjected to a set of constraints (or cuts) designed to define the geometry of the spectrometer and to reduce background. Secondly, sources of random and prompt background were identified and the appropriate subtractions performed.

A. Constraints

In the first analysis of the data, all constraints (cuts) were determined solely from the experimental distributions. In the reanalysis, in order to further reduce background, some of the constraints were tightened after comparing the experimental and simulated distributions (see Sec. S IV).

The following variables were routinely constrained in all experimental and simulated data: (1) the wire chamber coordinates, (2) the longitudinal and vertical vertex coordinates, (3) the horizontal and vertical vertex errors, (4) the azimuthal angle of the left proton, (5) the detected proton energies (applied to the simulated data only), and (6) a goodness-of-fit parameter χ^2. Additional cuts on the relative noncoplanarity ϕ_r, Harvard photon angle ψ_γ, and proton polar angles θ_L and θ_R were imposed as required by the particular analysis being performed.

B. Goodness-of-fit parameter

It has been a common practice in previous ppB experiments to select good events directly from an E_1-E_2 scatter plot. Due to the large solid angles used in this experiment with the consequent kinematic broadening, it was useful to define a goodness-of-fit parameter χ^2 as follows:

$$\chi^2 = (E_F - E_I)^2/(\Delta E_F)^2 . \tag{7}$$

Here E_F is the total final state energy calculated from the measured proton angles and energies using momentum conservation, E_I is the same quantity obtained from the known energy of the incident beam, and ΔE_F is the calculated uncertainty in E_F obtained by compounding the measured resolutions in the proton angles and energies. More details of this procedure can be found in T1 and P1. Since this procedure has never before been used in low energy bremsstrahlung experiments, it is best explained by an example. In Fig. 11 a series of scatter plots of E_L vs E_R for a small set of ppB events is shown. The angular ranges chosen were $44° < \theta_S < 52°$, $4° < \theta_D < 6°$, and $\phi_r < 0.4$, since these correspond approximately to the region where the detection efficiency was maximized, the background was average, and the kinematic broadening was minimized. Figures 11(a) and 11(b) show the prompt and random events, respectively. These events have passed all of the cuts except the χ^2 cut. The expected concentration of ppB events near the kinematic ellipse is seen. In part (a), the diagonal band in the upper right corner corresponds to $^2\mathrm{H}(p, 2p)n$ events. In Figs. 11(c) and 11(d) the distributions of the real (prompt less random) events for $\chi^2 \leq 4.36$ and $\chi^2 > 4.36$, respectively, are shown. It is clear that the effect of the χ^2 cut is to select events near the proper kinematic ellipse for the measured proton angles. In Fig. 12, the χ^2 distribution for the events depicted in 11(a) and 11(b) are shown. The sharp peak for $\chi^2 \approx 0$ in the prompt events is due to the ppB events.

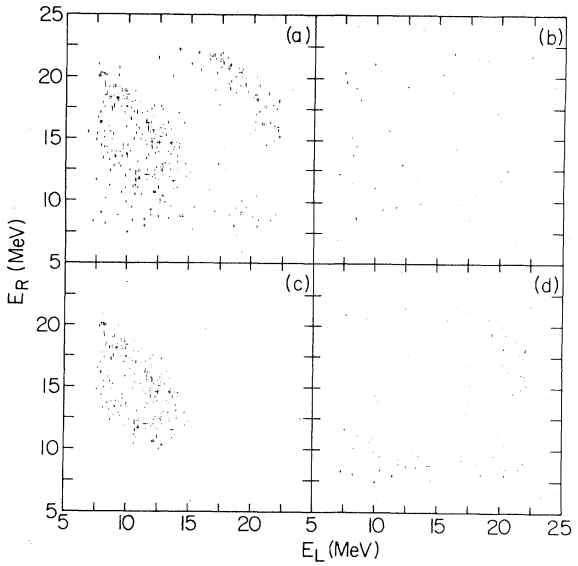

FIG. 11. Scatter plots of a sample of events in the E_L-E_R plane illustrating the usefulness of the χ^2 constraint in the process of data selection. The events plotted have been selected on all standard constraints and the following angular constraints: $4° < \theta_D < 6°$, $44° < \theta_S < 52°$, and $\phi_r < 0.4$. In parts (a) and (b), all prompt and random events are shown, respectively. In parts (c) and (d), the real (prompt minus random) events are shown for $\chi^2 \leq 4.36$ and $\chi^2 > 4.36$, respectively.

C. Background

Information from the χ^2 distributions proved to be very useful in analyzing the data for background contamination. In Fig. 13(a), the open circles give the χ^2 distribution for all prompt events collected in Exp. II. The existence of a large tail indicates a significant background contribution. In addition to the random background, four sources of prompt background were identified; the baffles, degraded elastic events, pile-up coincidences, and

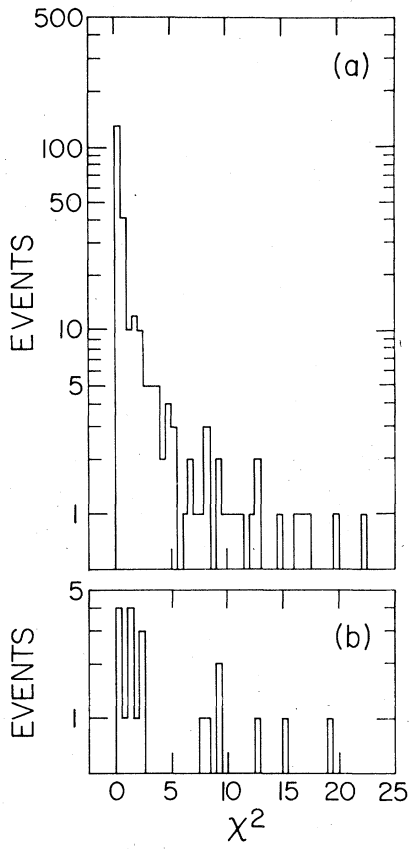

FIG. 12. The χ^2 distributions are shown for the samples of prompt (part a) and random (part b) events displayed in Figs. 11(a) and 11(b).

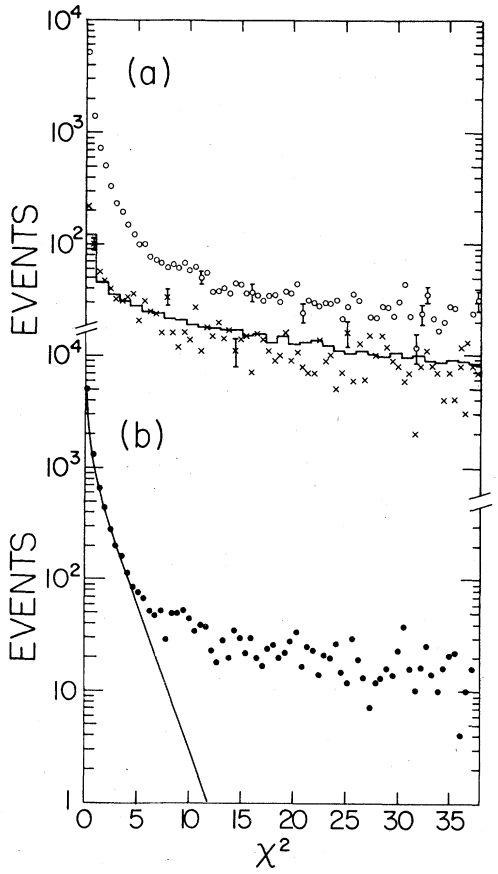

FIG. 13. χ^2 distributions for the entire sample of ppB events obtained in Exp. II. In part (a), the distributions due to all prompt (open circles) and random (crosses) events are shown. The histogram represents the distribution of random events simulated by the program RANDEV. The simulated histogram was normalized to the experimentally measured random events by requiring that the area under the histogram be equal to the sum of all random events shown in this figure. In part (b), the difference between the prompt and random event distributions is shown. The heavy line is the expected χ^2 distribution for one degree of freedom assuming a Gaussian distribution. The presence of a tail due to prompt background is obvious.

impurities in the target gas. In Table IV, the numbers of prompt ppB candidates and random and prompt background events as a function of the polar angle bin (see Sec. VIII) are summarized.

1. Random background

During data taking, random events were recorded in parallel with prompt coincidence events. The prompt and random data were analyzed under identical conditions and a simple subtraction was made on a bin by bin basis.

In Fig. 13(a), the χ^2 distribution for random events is shown by the crosses. For large values of χ^2, the distribution is flat, while for small χ^2, it exhibits a definite peak. In order to understand this behavior, a data simulation program RANDEV was written to simulate elastic random events which had their detected energies degraded through nuclear interactions in the scintillation counters.[32] These events were generated over the full angular range subtended by the spectrometer and were weighted according to the $d\sigma/d\theta$ elastic cross sections. The results are shown as the histogram in Fig. 13(a). This has been normalized to the experimental data so that the areas under the two distributions are the same. The fact that the simulated data also peaks for small χ^2 indicates that the effect is real.

In Fig. 13(b), the χ^2 distribution of prompt events with randoms subtracted is shown. The heavy line represents the expected χ^2 curve for one degree of freedom. The large tail indicates the presence of some prompt background.

TABLE IV. The number of events in Exp. II used in the conventional analysis of the data as a function of angular bin.

θ_D	θ_1-θ_2	Prompt events	Random background	Prompt background
	18-18	371	96	41
	22-22	632	41	73
0°	26-26	576	12	47
	30-30	392	3	15
	34-34	178	1	2
	18-22	833	94	96
	22-26	1059	73	123
4°	26-30	881	17	59
	30-34	538	3	19
	34-38	202	1	1
	18-26	514	42	78
	22-30	678	26	88
8°	26-34	507	3	28
	30-38	239	1	3
	18-30	217	6	36
12°	22-34	313	4	34
	26-38	146	3	7
16°	18-34	59	4	12
	22-38	67	5	10
		8402	435	772

2. Baffles

The baffles $B1$ and $B2$ (see Fig. 1) constituted potential sources of prompt background events. In other bremsstrahlung experiments,[8] this kind of background has been termed "slit scattering background" and only in the last Oak Ridge experiment[35] was it dealt with. In this experiment, with the help of the vertex reconstruction procedures, it was observed and entirely eliminated by restricting the length of reaction volume away from the baffles $B1$ and $B2$.

3. Degraded elastics

A second source of prompt background originated from degraded pp elastic events. These events were elastic scattering events in which one proton was directly recorded in one spectrometer arm but had its energy degraded through a nuclear reaction in the scintillator, while the second proton was scattered from a carbon atom in the 50 μm Mylar foil so that it was recorded in the second spectrometer arm. Such events could simulate true ppB events, except that their vertex error distribution was much broader, hence they could be identified and rejected. It was determined that the maximum contribution to any polar angle bin from such events was less than 1%.

4. Pile-up coincidences

Another source of prompt background was due to miscellaneous pp, np, or nn coincidences which were misinterpreted at the PDP-15 level due to extra random tracks in the wire chambers. The effects of pp and nn events were small; the background was due primarily to np and pn coincidences with a spurious track occurring in the hodoscope which detected the neutron. Vertex constraints eliminated approximately 95% of these events and the χ^2 constraint eliminated an additional 90%. Thus, the overall contamination after all constraints were applied was estimated to be between 1 and 2% of the prompt ppB sample.

5. (p,2p) events from target impurities

The most important source of prompt background was due to $(p, 2p)$ reactions on contaminants in the hydrogen gas. Impurities in the target gas were estimated to be on the order of 100 ppm. However, the $(p, 2p)$ cross sections on reactions from common impurities (oxygen, nitrogen) are generally three orders of magnitude larger than the corresponding ppB cross sections, hence the contamination due to $(p, 2p)$ reactions was expected to be on the order of 10%.

In order to determine the amount of background present, a separate experiment was performed in which the scattering chamber was filled with nitrogen, helium,[36] or air. Data were taken and analyzed in the same manner as the ppB data. In Figs. 14(a) and 14(b), the missing mass distributions of events taken with nitrogen and hydrogen target gas, respectively, analyzed as ppB events, and selected to have $10 < \chi^2 < 50$ are shown. In Fig. 14(a), the peaks due to the carbon ground state and the first few excited states can be identified. The distribution in Fig. 14(b) shows some peaks in different positions and of somewhat different heights, thus indicating that the prompt background is not coming exclusively from nitrogen impurities, but, presumably, also from oxygen and, to a lesser extent, other contaminants.

It was assumed that the χ^2 dependence of the prompt background was the same as for the nitrogen target gas.[37] The number of pure ppB events N^{ppB} was then computed from

$$N^{ppB} = N_p^{ppB} - N_r^{ppB} - K(N_p^N - N_r^N), \tag{8}$$

where N_p^{ppB}, N_r^{ppB}, N_p^N, and N_r^N denote the number of measured prompt and random ppB candidate and nitrogen events, respectively, and K is a normalizing constant.

One obvious way to determine K was to demand that χ^2 distributions of prompt minus random events for the ppB and nitrogen data agree for

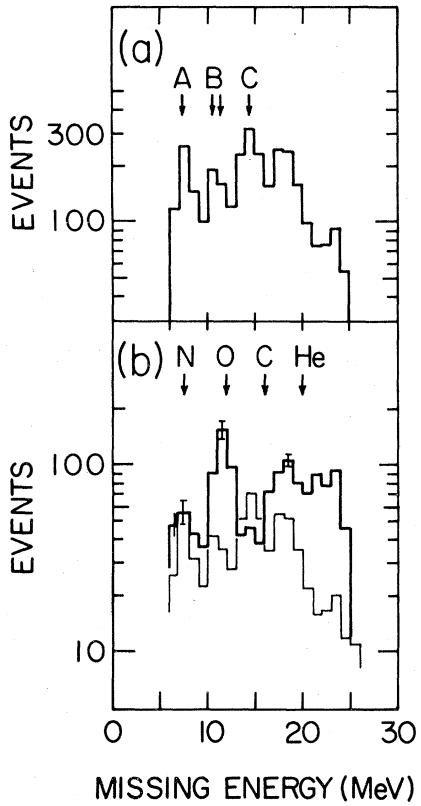

FIG. 14. (a) The missing mass distribution for the data taken with a nitrogen gas target. The events were processed as ppB events and selected to have χ^2 between 20 and 50. The arrow A indicates the position of the ground state in ^{13}C, the arrows B indicate the positions of the 3.09, 3.68, and 3.85 MeV excited states and the arrow C indicates the position of the 6.86 MeV excited state. The peak at 18 MeV is presumably due to excited states at 10–11 MeV which cannot be individually identified. (b) The heavy line histogram represents ppB data selected to have χ^2 between 20 and 50. The light line has been replotted from part (a) and is normalized to the ppB histogram at the 7.5 MeV point. The arrows labeled N, O, C, and He indicate the position of the ground states for the $(p,2p)$ reaction on nitrogen, oxygen, carbon, and helium, respectively.

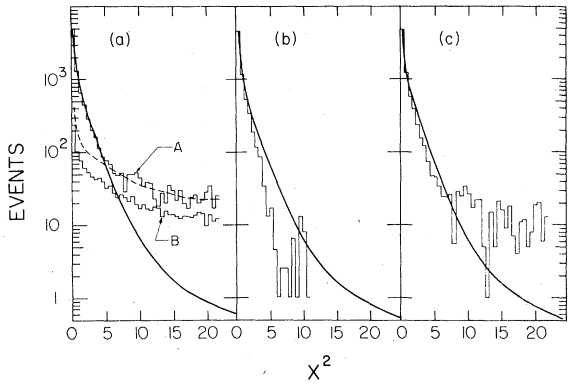

FIG. 15. (a) The top histogram (A) is the χ^2 distribution of prompt minus random events from Exp. II replotted from Fig. 13(b). The heavy line represents the smoothed out χ^2 distribution for simulated events (see Sec. IV E in S) normalized so that the numbers of events in the first two channels of the simulated and measured distributions are the same. The heavy lines in parts (b) and (c) have the same meaning. The bottom histogram (B) corresponds to the net prompt events taken with an N_2 gas target. This data has been normalized to the ppB data as shown in Fig. 14(b). The dashed line represents a smoothed out χ^2 distribution for N_2 events (histogram B) but normalized so that the numbers of nitrogen and ppB events in the χ^2 range between 10.8 and 21.8 are equal. (b) The difference between histogram A and the dashed line shown in part (a). (c) The difference between histograms A and B shown in part (a). This represents the fully subtracted sample of ppB events used in the conventional analysis.

large values of χ^2. This was done by requiring that the histograms A and B in Fig. 15(a) have the same number of events for $10.8 < \chi^2 < 21.6$. This yields a value of 0.419 for K.

A second method for evaluating K, and the one which was used in the analysis, was to require that the ground state carbon peak from the nitrogen reaction in both the ppB event sample and the nitrogen event sample be equal to each other. This requires that the peaks in the two distributions at 7.5 MeV shown in Fig. 14(b) be equal to each other. This gives a value of 0.223 for K.

The results are shown in Fig. 15. In the first panel the χ^2 distributions for the real ppB, nitrogen, and simulated events are shown. In the second and third panels, the χ^2 distributions of the net ppB events as defined by Eq. (8) using $K = 0.419$ and 0.223, respectively, are shown. The heavy line has the same meaning as previously explained. In the first case, $K = 0.419$, the background is clearly overestimated. In the second case, the agreement is reasonable for $\chi^2 < 8$ with the simulated distribution being somewhat wider, presumably due to overestimation of the multiple scattering in the simulated data.[38] On the other hand, the light line histogram in Fig. 14(b) is below the ppB histogram, which might indicate that the prompt background is being underestimated by setting $K = 0.223$, and that a mixture of data from the nitrogen and oxygen target gas should have been used. Although such a sophisticated background subtraction procedure might have been more appealing to perform, it was felt that the purity of the net ppB sample would not be any more reliable, as it would be impossible to prove that all prompt background is coming *only* from the nitrogen and oxygen impurities, and that the χ^2 distribution for $\chi^2 < 5.41$, in fact, has the same shape as that due to nitrogen and/or oxygen

targets.

Because the prompt background is only on the order of 10% and, in most cases, the statistical errors were of the same order or larger, it was judged that a sufficiently accurate procedure was to use the normalizing constant $K=0.22$ and to assign to it a rather large asymmetric error of +50% and −25%. In most cases the effect of error in K on the data was smaller than either the statistical error or the error due to the energy calibration of the scintillation counters (see Secs. VIII D and IX D).

TABLE V. Factors used in the normalization of the ppB cross section.

Quantity	Units	Exp. I	Exp. II
$(d\sigma/d\Omega)_{pp}$	mb/sr	29.8 ± 1%	29.8 ± 1%
l_{pp}	mm	4.20 ± 1.5%	4.20 ± 1.5%
$\Delta\Omega_{pp}$	msr	0.296 ± 1.7%	0.324 ± 1.9%
ϵ_{pp}		0.92 ± 3%	0.97 ± 3%
N_{pp}	events	207 502 ± 0.22%	453 771 ± 0.15%
R	cm^3	0.607×10^{35} ± 4%	1.15×10^{35} ± 4%

VII. CROSS SECTION NORMALIZATION

A. Method

The normalizing constant R was defined in Eq. (5) as the time integral of the product of four quantities. Since it was not practical to monitor these quantities during the experiment, the absolute normalization of the ppB cross sections was obtained indirectly. It was determined by detecting pp elastic events simultaneously with the ppB data, making the measurement of the ppB cross sections relative to the known pp elastic cross section $(d\sigma/d\Omega)_{pp}$. Because the pp elastic cross section is several orders of magnitude larger than the ppB cross section, it was sufficient to collect the pp elastic data from a very restricted range, l_{pp}, of the hydrogen target and over a very small solid angle $\Delta\Omega_{pp}$.

Due to the small sizes of l_{pp} and $\Delta\Omega_{pp}$, the total number of pp elastic events N_{pp} collected throughout the ppB experiment can be written in the form

$$N_{pp}=l_{pp}R\epsilon_{pp}\left(\frac{d\sigma}{d\Omega}\right)_{pp}\Delta\Omega_{pp}\,, \tag{9}$$

where ϵ_{pp} is the detection efficiency of the spectrometer for pp elastic events. The quantities l_{pp}, $\Delta\Omega_{pp}$, ϵ_{pp}, and $(d\sigma/d\Omega)_{pp}$ were evaluated directly, so that R was obtained from Eq. (9). The resulting value was then substituted into Eq. (3). A summary of the measurements used in evaluating Eq. (9) is given below; additional details can be found in T4. The values of all relevant quantities are listed in Table V.

B. Determination of the normalizing factor

The geometrical arrangement used to detect the pp elastic events is shown in Fig. 1. The pp elastic events originated from the very downstream end of the scattering chamber and were detected in coincidence, each of the protons making an average angle of 44.7° with the incident beam direction. The effective length l_{pp} of the hydrogen gas target was determined by the width of the narrow slit in the right hand side of the baffle $B2$. The solid angle $\Delta\Omega_{pp}$ was determined by the size of the slit in the baffle $A1$ situated in front of the scintillation counter S_R (cf. T4). On the left hand side of the spectrometer, no baffles were used so that all pp elastic events whose right hand proton was within $\Delta\Omega_{pp}$ were detected. l_{pp} and $\Delta\Omega_{pp}$ were chosen so as to give pp elastic trigger rates of about 3 events/sec nA. The elastic cross section at 42 MeV was obtained by interpolating from the results contained in Ref. 39.

The pp elastic events detected during each of the two experiments were processed on-line in the same manner as the ppB data. These events were selected solely on the basis of their longitudinal vertex position and wire chamber coordinates in the back right wire chamber; no attempt was made to select events on the basis of vertex errors, χ^2 or proton energy. This was possible because the origins of the ppB events and the pp elastic events within the target were well separated.

The precise determination of the efficiency factor ϵ_{pp} was the most difficult aspect in determining R. Since it was impractical to calculate ϵ_{pp} analytically, it was measured in a separate experiment. This was done by detecting pp elastic events in coincidence, using the same geometrical arrangement as in the data taking with the following exceptions: (1) the wire chambers were not triggered, and (2) in order to avoid unwanted background, the right scintillator was completely covered with brass plate sufficiently thick to stop 50 MeV protons (except for the diagonal slit) and a baffle was placed inside the scattering chamber in such a manner as to allow only protons passing through the slit in the $B2$ baffles to enter the right detector. Since the wire chambers were not triggered in this experiment, the system dead time was very small, and it was possible to correct for it. Also, the total charge was measured in a Faraday cup situated at the end of the beam line. Details of these corrections are given in T4. The background arising from np and nn coincidences

was also measured by blocking off completely one or both of the scintillators.

VIII. CONVENTIONAL ANALYSIS AND RESULTS

The relationship between the ppB cross sections and the number of ppB events detected in the experiment was defined by Eq. (3). The object of the conventional analysis was to extract the experimental cross sections using this equation. The procedures used and results obtained are presented in this section.

The data from Exp. II was analyzed twice in this manner, the first of which was reported in L2. After publication of these results, the systematic errors were reexamined in detail and the conventional cross sections recomputed.

To avoid confusion between the different cross sections discussed below, the following notation is used: σ^{TH} refers to the cross sections calculated from theory, σ^{EXP} refers to the cross sections determined from the experimental data, and σ^{SIM} refers to the cross sections determined from the simulated data. The last two cross sections may be expressed either in terms of the experimental or randomized variables (that is, with resolution and binning effects folded in) as $\sigma(\vec{q})$ or in terms of the theoretical or nonrandomized variables (that is, with resolution and binning effects unfolded) as $\sigma(\vec{q})$.

A. Method

It was not possible to solve Eq. (3) for $d\sigma/d\vec{q}' \equiv \sigma^{EXP}(\vec{q}')$ rigorously; certain approximations had to be introduced. The method adopted here was to assume a definite model for the cross sections and to use it in solving Eq. (3).

Equation (3) can be rewritten in the form

$$\Delta N^{ppB}(\vec{q}_0) = lR\,\Delta\vec{q}\,\alpha(\vec{q}_0)\sigma^{EXP}(\vec{q}_0)\,, \tag{10}$$

where

$$\alpha(\vec{q}_0) = \frac{1}{\Delta\vec{q}} \int_{\Delta\vec{q}} d\vec{q} \int_{all} d\vec{r}' \int_{all} d\vec{q}' \iint_{spec} K(\vec{q}'\vec{r}';\vec{q},\vec{r},\vec{s})\, \frac{\sigma^{EXP}(\vec{q}')}{\sigma^{EXP}(\vec{q}_0)}\, d\vec{r}\, d\vec{s} \tag{11}$$

and $\vec{q}_0$ is the central point of the bin $\Delta\vec{q}$. An identical expression can be written for the simulated data. Thus, if $\Delta N^{HIT}(\vec{q}_0)$ denotes the number of simulated events detected by the spectrometer in the range $\Delta\vec{q}$, then

$$\Delta N^{HIT}(\vec{q}_0) = lR\,\Delta\vec{q}\,\alpha^*(\vec{q}_0)\sigma^{SIM}(\vec{q}_0)\,, \tag{12}$$

where

$$\alpha^*(q_0) = \frac{1}{\Delta\vec{q}} \int_{\Delta\vec{q}} d\vec{q} \int_{all} d\vec{r}' \int_{all} d\vec{q}' \iint_{spec} K(\vec{q}',\vec{r}';\vec{q},\vec{r},\vec{s})\, \frac{\sigma^{TH}(\vec{q}')}{\sigma^{SIM}(\vec{q}_0)}\, d\vec{r}\, d\vec{s}\,. \tag{13}$$

Note that both Eqs. (11) and (13) contain the effects of all cuts placed on the data including χ^2, vertex errors, etc. Without imposing these cuts we get ΔN^{TOT}, the total number of events actually generated in the range $\Delta\vec{q}$,

$$\Delta N^{TOT}(\vec{q}_0) = lR\,\Delta\vec{q}\,\alpha'(\vec{q}_0)\sigma^{SIM}(\vec{q}_0)\,, \tag{14}$$

where $\alpha'(\vec{q}_0)$ is given by an expression identical to (13) except that the range of integration over $d\vec{r}\,d\vec{s}$ covers all possible values except for the longitudinal vertex position which is integrated over the length of the target. In practice, $\alpha'(\vec{q}_0)$ is very nearly equal to one, the only deviations arising from cross talk between adjacent bins, which does not necessarily cancel. Dividing Eq. (12) by (14) then gives

$$\frac{\alpha^*(\vec{q}_0)}{\alpha'(\vec{q}_0)} = \frac{\Delta N^{HIT}(\vec{q}_0)}{\Delta N^{TOT}(\vec{q}_0)}. \tag{15}$$

$\alpha(\vec{q}_0)$ was evaluated by making the identification

$$\alpha(\vec{q}_0) = \frac{\alpha^*(\vec{q}_0)}{\alpha'(\vec{q}_0)}\,. \tag{16}$$

Substitution of (16) and (15) into (10) gives

$$\sigma^{EXP}(\vec{q}_0) = \frac{\Delta N^{ppB}(\vec{q}_0)}{lR\,\Delta\vec{q}}\,\frac{\Delta N^{TOT}(\vec{q}_0)}{\Delta N^{HIT}(\vec{q}_0)}\,. \tag{17}$$

for the experimental cross sections.

Equation (16) is, in principle, the weakest part of this procedure, since it assumes that $\sigma^{TH}(\vec{q}')/\sigma^{SIM}(\vec{q}_0)$ provides an accurate representation of the ratio of the true ppB cross sections. To the extent that this assumption is not satisfied, the experimental results will depend on the theoretical model chosen as input. This is the meaning of the closed loop referred to in Sec. II and depicted in Fig. 3. In our case, this dependence is relatively

weak (cf. Sec. VIII D 6). In addition, implicit in this procedure is the assumption that simulated (randomized) variables are an accurate representation of their experimental counterparts. Evidence to this effect is presented in Sec. S IV.

The cross sections obtained from Eq. (17) are not directly comparable to the theoretical cross sections listed in Sec. S VI because of resolution and binning effects. To make a valid comparison between the two sets of cross sections, either the resolution and binning effects had to be folded into the theoretical cross sections, or the experimental ones had to be corrected for them. Both approaches were used in the conventional analysis.

Inverting Eq. (14), assuming $\alpha'(\vec{q}_0)$ is equal to one, and then solving for $\sigma^{\mathrm{SIM}}(\vec{q}_0)$, gives the theoretical cross sections with all binning and resolutions folded in and, thus, in a form which can be compared directly with the experimental cross sections. In this context, it should be pointed out that in evaluating $\sigma^{\mathrm{SIM}}(\vec{q}_0)$ using Eq. (14), it is necessary to normalize the simulated data to the experimental data. The procedure used to do this is described in Sec. VIII B 2.

The inverse procedure, that of unfolding the resolution effects from the experimental cross sections, was accomplished using the relation

$$\sigma^{\mathrm{EXP}}(\vec{q}_0') = \frac{\sigma^{\mathrm{TH}}(\vec{q}_0')}{\sigma^{\mathrm{SIM}}(\vec{q}_0)}\,\sigma^{\mathrm{EXP}}(\vec{q}_0)\,. \tag{18}$$

This simple relationship clearly introduces some additional dependence on the theoretical input.

In this experiment, comparison between $\sigma^{\mathrm{EXP}}(\vec{q}_0)$ and $\sigma^{\mathrm{SIM}}(\vec{q}_0)$ is influenced the least by the theoretical input, thus in Sec. S VII both of these cross sections are listed. However, in order to facilitate comparison of the experimental data from this experiment with possible future calculations utilizing different theoretical models, the $\sigma^{\mathrm{EXP}}(\vec{q}_0')$ cross sections are also computed using Eq. (18) and listed in Sec. S VII.

Finally, it should be noted that the problem of theoretical input outlined above has been present in all ppB experiments performed to date, although it may not have been dealt with explicitly.

B. Evaluation of cross sections

Three different sets of cross sections were computed[40] in the conventional analysis, namely $d^3\sigma/d\Omega_1 d\Omega_2 d\psi_\gamma$, $d^2\sigma/d\Omega_1 d\Omega_2$, and $d^2\sigma/d\theta_1 d\theta_2$ using the programs EXPCROSS and EXPSUM (see Sec. S I of Ref. 23). The data was stored in the form of eight four-dimensional arrays, each of the form N_{ijkl}, corresponding to real and random ppB events, real and random nitrogen events, and "total" and "hit" simulated events, both weighted and unweighted. The indices i, j, k, l were used to define the appropriate angular bin. The data was binned in 4° ranges in both proton polar angles (corresponding to the indices k and l) covering 16°–36° in θ_R and 16°–40° in θ_L. Bins with the same values of θ_S and θ_D were combined.[41] The indices i and j defined an 18×20 matrix covering a 0°–360° range in ψ_γ (20° bins) and 0–2.0 range in ϕ_γ (0.1 bins). The range in ϕ_γ was extended to 2.0 to allow for effects of the spectrometer resolution.

1. Experimental cross sections

The fivefold differential cross sections were calculated from the expression

$$d^3\sigma_{ikl}^{\mathrm{EXP}} = \sum_{j=1}^{7} N_{ijkl}^{\mathrm{ppB}} \,/\, [7lR\alpha_{ikl}\,\Delta(\cos\Theta_1)\Delta(\cos\Theta_2)\Delta\phi_1 2\phi_{DM}\Delta\phi_\gamma\Delta\psi_\gamma]\,, \tag{19}$$

where R is the normalizing constant discussed in Sec. VII, l is the nominal target length, and α_{ikl} is the correction factor obtained from Eqs. (15) and (16), i.e.,

$$\alpha_{ikl} = \sum_{j=1}^{7} N_{ijkl}^{\mathrm{HIT}} \Big/ \sum_{j=1}^{7} N_{ijkl}^{\mathrm{TOT}}\,. \tag{20}$$

In calculating $d^3\sigma_{ikl}^{\mathrm{EXP}}$ from Eq. (19), the number of ppB events has been summed over the first seven bins in ϕ_γ (i.e., from 0.0 to 0.7). This was done in order to improve statistics. This procedure is justified if the cross sections are relatively flat over the range in question and if α_{ikl} is calculated from distributions which are similar to the experimental data. The theoretical calculations show (see Figs. 4 and 5, in Sec. S VI) that, in general, the $d^2\sigma/d\Omega_1 d\Omega_2$ cross sections are moderately flat as a function of ϕ_γ for $\phi_\gamma < 0.7$.

In the case of symmetric polar angle bins, the $d^3\sigma$ cross sections are symmetric with respect to $\psi_\gamma = 180°$. Therefore, the experimental $d^3\sigma$ cross sections were expressed only for ψ_γ in the range from 0° to 180°. This was done by first computing the $d^3\sigma$ cross sections for all 18 bins in ψ_γ and then by taking a weighted average of pairs symmetric with respect to $\psi_\gamma = 180°$.

The $d^2\sigma/d\Omega_1 d\Omega_2$ cross sections were obtained directly from the data stored on disk using the expression

$$d^2\sigma_{jkl}^{\mathrm{EXP}} = \sum_{i=1}^{18} N_{ijkl}^{\mathrm{ppB}} / (lR\alpha_{jkl}\Delta(\cos\theta_1)\Delta(\cos\theta_2)\Delta\phi_1 2\phi_{DM}\Delta\phi_r), \quad (21)$$

where

$$\alpha_{jkl} = \sum_{i=1}^{18} N_{ijkl}^{\mathrm{HIT}} \Big/ \sum_{i=1}^{18} N_{ijkl}^{\mathrm{TOT}} . \quad (22)$$

By summing Eq. (21) over j, the $d^2\sigma/d\theta_1 d\theta_2$ cross sections were obtained as follows:

$$d^2\sigma_{kl}^{\mathrm{EXP}} = \left(\frac{\pi^2}{900}\right)\phi_{DM}\sin\theta_1\sin\theta_2 \sum_{j=1}^{14} d^2\sigma_{jkl}^{\mathrm{EXP}} . \quad (23)$$

The limit of $j=14$ ($\phi_r=1.4$) on the summation over ϕ_r was a compromise. As mentioned previously, resolution effects spread the data out to nearly 2.0 in ϕ_r with anywhere from 1–3% of the events having $\phi_r > 1.4$. However, for $\phi_r > 1.4$, the effects of prompt background completely mask the data so that its inclusion becomes meaningless. The Monte Carlo correction factor α_{jkl} compensated for data lost through this cut.

2. *Simulated cross sections*

The simulated cross sections were calculated from Eq. (14), but utilizing a different normalization constant, R_s. This was equivalent to replacing N_{ijkl}^{ppB} in Eqs. (19), (21), and (23) by N_{ijkl}^{HIT} as well as replacing R by R_s. R_s was obtained by requiring that the cross sections determined from the nonrandomized simulated data averaged over a large range of polar angle bins, agree with the results of the theoretical calculation averaged over the same regions of polar angles. The particular choice of bins, 18°–38°, 18°–34°, 18°–30°, 18°–26°, 22°–38°, and 22°–34°, was used because in these ranges the $d^2\sigma/d\theta_1 d\theta_2$ cross sections were relatively linear, thus minimizing the in-scattering and out-scattering effects caused by the finite bin size.

3. *Quoted errors*

The errors quoted with the data include both statistical and some systematic effects. The statistical errors were obtained in the usual manner by combining the errors in the number of prompt, background, and simulated events.

Two different systematic effects were included with the statistical errors. The first arose from the fact that the number of events in some bins was so small that the cross sections and the corresponding errors should have been determined by using the method of maximum likelihood. Since the data did not justify such an elaborate error analysis and since the Poisson distribution is wider than the Gaussian distribution for a small number of events, the error on all bins with less than 5 (net ppB) events was doubled, while for bins with less than 10 (15) events, the error was increased by a factor of 1.5 (1.2). This correction affected points primarily in the ψ_γ distributions; the only points in the ϕ_r distributions affected occurred in the tails.

The errors quoted with the data were also increased to allow for energy dependent biases. It has been pointed out in Sec. V that below approximately 10 MeV there was some uncertainty in the energy calibration. χ^2, the vertex errors, angular resolution, and the software cutoffs on the simulated data all depended on the knowledge of the energies of the final state protons. The method adopted to compensate for the uncertainty in these biases was to calculate first a purely geometrical correction factor γ. This was determined using the program TEETH (see Sec. SIB) solely on the basis of whether or not the protons hit the wire chambers; those which passed through the sensitive area of the chambers were accepted, all others were rejected. This geometric correction was compared with the full Monte Carlo correction factor α. The ratio of these two quantities, $\beta = \alpha/\gamma$, then provided a measure of the energy dependent correction factor. If β was greater than 1.25 (1.50) for Exp. I (II), the error was increased by 50%. If β was greater than 1.5 (2.0), the data was rejected outright. The more severe restrictions were applied to the earlier data because the pulse height energy calibration curve was based on a smaller number of points and was considered less reliable. This criterion was applied on a point by point basis to the ψ_γ distributions and on an average basis ($0 < \phi_r \leq 1.0$) to the ϕ_r distributions. Thus, the ϕ_r distribution for a given set of polar angles was either completely accepted or rejected, whereas individual points were accepted or rejected in the ψ_γ distributions. A plot of β as a function of both ψ_γ and ϕ_r for a typical polar angle bin is shown in Fig. 16. The factor β is shown separately for Exp. I and Exp. II in order to emphasize the much greater effect of the energy dependent biases in Exp. I.

C. Results

All experimental and simulated results are presented in numerical form in Table VI and Sec. S VII. The experimental data is presented both without and with the corrections for resolution and binning. The simulated data has all resolutions folded in and has been modified to compensate for the error in determining the angular

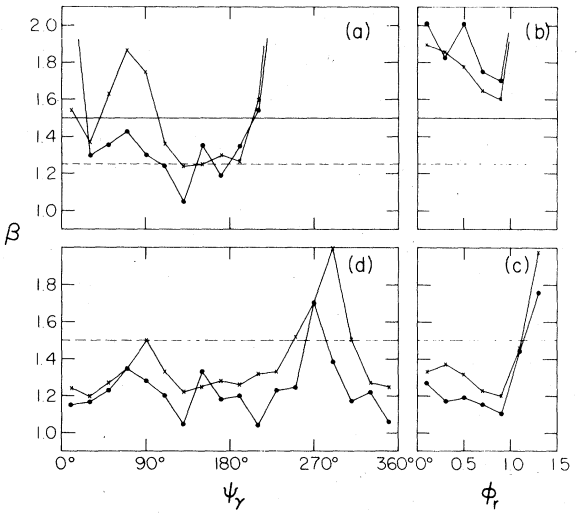

FIG. 16. The energy dependent correction factor β (see text) is plotted as a function of ψ_γ and ϕ_r for $\theta_L = 22°$, $\theta_R = 26°$(×)and $\theta_L = 26°$, $\theta_R = 22°$(•). Figures (a) and (b) show the correction factors used in Exp. I and Figs. (c) and (d) those used in Exp. II. The dashed and solid horizontal lines [in parts (c) and (d) the solid line is at $\beta = 2.0$] represent the limits beyond which the errors on the corresponding cross sections were either increased by 50% or the data was rejected altogether.

resolution using the procedure described in Sec. SIV A. In addition to the errors quoted with the data, there is an additional uncertainty of ±4% (see Table V) due to the error in the determination of the normalizing constant R.

The cross sections from Exp. I and Exp. II were calculated separately and then combined on a point by point basis. In Sec. SVIII, the combined results for the $d^3\sigma/d\Omega_1 d\Omega_2 d\psi_\gamma$ and $d^2\sigma/d\Omega_1 d\Omega_2$ cross sections as determined from the first analysis are given. Changes in the results arising from the reanalysis of the data were not considered significant enough to warrant their inclusion.

Representative examples of the $d^3\sigma/d\Omega_1 d\Omega_2 d\psi_\gamma$ and the $d^2\sigma/d\Omega_1 d\Omega_2$ cross sections are shown in Figs. 17 and 18, respectively. (The complete set of $d^3\sigma/d\Omega_1 d\Omega_2 d\psi_\gamma$ and $d^2\sigma/d\Omega_1 d\Omega_2$ cross sections[42] is shown in Fig. 6 of Ref. 9.) In each case, the solid histograms correspond to $\sigma^{\mathrm{SIM}}(\vec{q}_0)$, i.e., the cross sections as determined from Eq. (14) with $\alpha'(\vec{q}_0)$ set equal to 1. The dashed histograms correspond to $\sigma^{\mathrm{SIM}}(\vec{q}_0')$, that is, the simulated cross sections expressed in terms of the nonrandomized variables. This means that no effects of resolution have been included, but binning has been. These histograms were obtained from the simulated data using the relation

$$\Delta N^{\mathrm{TOT}}(q_0') = lR\Delta q_0' \frac{1}{\Delta q'} \int_{\Delta q'} d\vec{q}'\sigma^{\mathrm{TH}}(\vec{q}') = lR\Delta q'\sigma^{\mathrm{SIM}}(\vec{q}_0') . \quad (24)$$

In Fig. 19, the ratio of the experimental $d^2\sigma/d\theta_1 d\theta_2$ cross sections to the simulated ones is shown as a function of θ_s for different values of θ_D. The data from Exp. I and Exp. II are shown separately in order to illustrate the extent of agreement between them. Although the data from Exp. I is somewhat higher than that from Exp. II (the weighted average of the ratio of the two sets is 1.07 ± 0.05), this is consistent with the uncertainty in the overall normalization. As with the higher order cross sections, the data presented for Exp. II is based on the first analysis. The extension of the error bars was based on a comparison of the first data analysis with the reanalyzed data. If the cross sections differed by more than 10% of the quoted error, this difference was added linearly to the error bars; if the difference was less than 10%, no adjustment was made to the data. In addition, the results from the McGill[43] and Orsay[44] experiments at 99 and 156 MeV are shown for comparison. These latter results are not fully integrated $d^2\sigma/d\theta_1 d\theta_2$ cross sections, but $d^2\sigma/d\Omega_1 d\Omega_2$ cross sections averaged over the appropriate regions of phase space. Furthermore, the theoretical models used for comparison of the McGill and Orsay data were not identical to the one described herein. All models were based on the H-J potential, but each included different corrections. No allowance for this has been made in Fig. 19.

D. Systematic errors

Several checks on the internal consistency of the data were made by calculating the $\sigma \equiv d^2\sigma/d\theta_1 d\theta_2$ cross sections using different analyzing conditions denoted A and B, and then forming the ratios $R = \sigma_A/\sigma_B$. The most important of these tests are described below and the results are presented in Fig. 20. In parts (a) and (b) of Fig. 20, σ_A and σ_B are statistically independent so that the error in R is given by $(\delta R/R)^2 = (\delta\sigma_A/\sigma_A)^2 + (\delta\sigma_B/\sigma_B)^2$. In parts (c), (e), and (f), the error in R is simply $\delta R = \delta\sigma_A/\sigma_B$.

For the $d^2\sigma$ and $d^3\sigma$ cross sections, the statistical errors were in general larger than any systematic effects; thus no special investigation of systematic errors at that level was done.

1. Effects dependent on beam intensity

In principle, it was possible that the spectrometer had some biases which were dependent on beam intensity. For this reason, the data were

TABLE VI. $d^2\sigma/d\theta_1 d\theta_2$ cross sections (nb/r^2). The experimental cross sections from the first analyses are listed in columns 3–5. They have been calculated using Eq. (23) and include the effects of resolution and binning. The extended errors obtained using the reanalyzed cross sections as discussed in Sec. IX C are shown in column 6. In column 7, the simulated cross sections calculated as explained in Sec. IX B2 are presented. Column 10 lists the experimental cross sections fully corrected for both resolution and binning effects using the procedure defined in Eq. (18). Columns 8 and 9 show separately the correction factors used to correct for resolution and binning effects. The best experiment to theory comparison of the data presented here is obtained by comparing the data in columns 5 and 7 (see Fig. 19). The data in column 10 is included so that the results of this experiment may be compared to other theoretical models in cases where it is not feasible to calculate the corresponding simulated cross sections.

		Experimental					Correction		
		Exp.	Exp.	[see Eq. (17)]	Extended	Simulated	for		Experimental
θ_D	θ_S	I	II	Avg.	errors	[see Eq. (14)]	resolution	binning	[see Eq. (18)]
0	36		265±45	265±45		333±4	1.123	1.021	303±51
	44		289±19	289±19	+26/−19	335±4	1.101	0.978	311+27/−20
	52	385±47	316±18	324±17		355±4	1.085	0.971	342±18
	60	414±34	391±23	398±19	+19/−32	395±4	1.081	0.951	409+20/−33
	68	522±61	444±38	465±32	+32/−43	458±5	1.109	0.929	483+32/−43
4	40		287±27	287±27	+37/−27	317±3	1.095	1.009	317+40/−30
	48		253±11	253±11		329±3	1.109	0.953	268±12
	56	380±35	339±14	345±13	+13/−38	352±3	1.094	0.969	366+14/−40
	64	379±31	389±21	386±17	+17/−51	407±3	1.108	0.945	404+18/−54
	72	581±74	595±49	591±41	+41/−52	506±6	1.109	0.930	609+42/−53
8	44		224±23	224±23	+56/−23	285±2	1.077	1.107	267+66/−27
	52		232±13	232±13	+13/−21	305±2	1.092	0.994	251+14/−23
	60	362±49	321±17	325±16	+16/−46	356±3	1.112	0.942	340+17/−47
	68	406±44	378±31	388±25	+25/−51	426±5	1.099	0.951	405+26/−53
12	48					253±2	1.087	0.964	
	56		220±19	220±19		292±2	1.096	0.966	232±20
	64		272±27	272±27	+27/−79	353±4	1.096	0.951	284+28/−82
16	52					224±2	1.063	0.996	
	60		173±46	173±46	+46/−79	277±3	1.079	0.997	186+49/−85

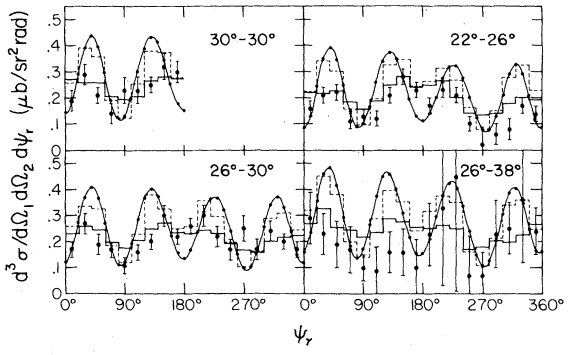

FIG. 17. The $d^3\sigma/d\Omega_1 d\Omega_2 d\psi_r$ cross sections for the polar angle bins indicated are presented as a function of the Harvard photon angle ψ_r. The data shown include all events which $\phi_r \leq 0.7$. The solid histograms give the simulated cross sections with resolution and binning effects folded in while the dashed histograms include only binning effects. The solid curve corresponds to the theoretical cross section evaluated at the central point of the polar angle bin for the (nearly) coplanar case (see Sec. S VI).

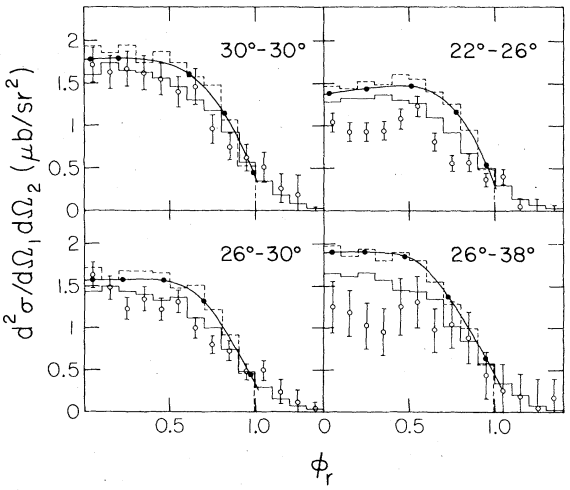

FIG. 18. The $d^2\sigma/d\Omega_1 d\Omega_2$ cross sections are shown as a function of the relative noncoplanarity ϕ_r. The histograms have the same meaning as in Fig. 17. The continuous heavy line represents the theoretical cross sections as given in Sec. S VI.

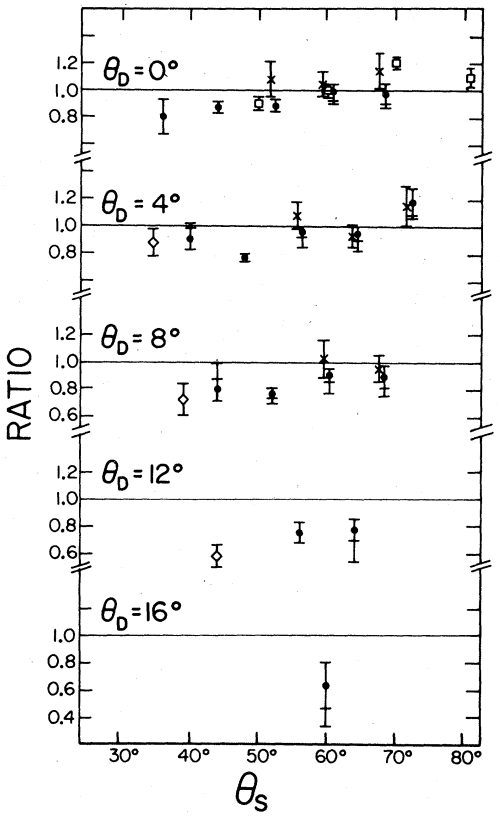

FIG. 19. The ratios of the experimental to the simulated $d^2\sigma/d\theta_1 d\theta_2$ cross sections are shown as a function of $\theta_S = \theta_1 + \theta_2$ for different values of $\theta_D = |\theta_1 - \theta_2|$. The data from Exp. I (×) and Exp. II (·) are shown separately to illustrate the extent of agreement between them. Also shown in a form suitable for comparison are the data from the Orsay (◇) and McGill (□) experiments. See text for the explanation of extended error bars.

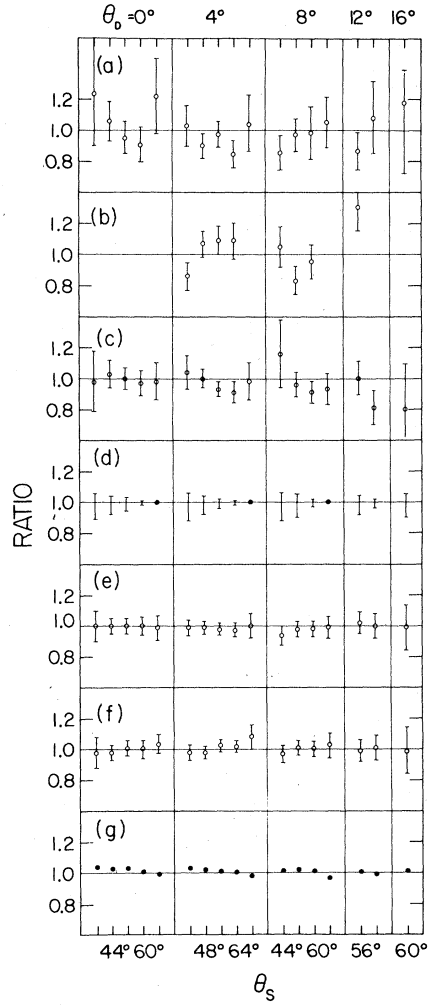

FIG. 20. A series of comparisons which were used to check the experimental data for possible systematic effects are presented. In each case [except (d)], the comparison was made by forming the ratio $R = \sigma_A/\sigma_B$ (see Sec. VIII D), where σ_A and σ_B denote second order differential cross sections calculated under the conditions denoted below. (a) σ_A and σ_B were determined from data collected using beam intensities of 1 nA and 3 nA, respectively; (b) σ_A and σ_B were determined from data binned with the same values of θ_S and θ_D, but with $\theta_L > \theta_R$ and $\theta_L < \theta_R$, respectively; (c) σ_A and σ_B were determined from the first analysis and the reanalysis of the data from Exp. II; (d) the maximum uncertainty in the prompt background subtraction as obtained from the data in Table IV and assuming that the maximum error in K [Eq. (8)] is +50%/−25%; (e) σ_A and σ_B were determined using $\Delta\phi_r = 0.2$ and 0.1, respectively; (f) σ_A was obtained by assuming that the theoretical dependence of the correction factors is given by the H-J potential and σ_B by assuming a phase space dependence; (g) σ_A denotes the theoretical cross sections evaluated in terms of the Harvard angles $\bar{\theta}_S (= \bar{\theta}_1 + \bar{\theta}_2)$, $\bar{\theta}_D (= |\bar{\theta}_1 - \bar{\theta}_2|)$ and σ_B denotes those evaluated in terms of the corresponding spherical polar angles θ_S and θ_D.

taken at two different beam intensities (1 nA and 3 nA), analyzed separately, and then checked for consistency. The results, shown in Fig. 20(a), are self-consistent.

2. *Asymmetry test*

As described previously, asymmetric polar angle bins with the same values of θ_S and θ_D were combined to improve statistics. Theoretically, these cross sections are identically equal to each other. Thus, one check on possible experimental biases was to see if the ratio of these cross sections was consistent with one. The results, presented in Fig. 20(b), show no statistically significant biases.

3. *The effect of the data reanalysis*

In Fig. 20(c), the ratios of the cross sections based on the reanalyzed data to those determined

from the first analysis are shown. For small values of θ_D, the agreement is quite good. However, for larger values of θ_D, the reanalyzed cross sections tend to be lower than those based on the original analysis. This increases the discrepancy between experiment and theory as indicated by the extension of the error bars in Fig. 19.

4. Prompt background subtraction

In Sec. VI C 5, it was estimated that the error in subtracting the prompt background due to impurities in the target gas was asymmetric, indicating that it was more likely that the background was underestimated rather than overestimated. In Fig. 20(d), the maximum error is shown on a bin by bin basis. This demonstrates that systematic effects from the prompt background subtraction could not account for the observed discrepancy. In fact, it is more likely that they would increase rather than decrease it.

5. Binning effects

Since the $d^2\sigma/d\theta_1 d\theta_2$ cross sections were calculated by integrating $d^2\sigma/d\Omega_1 d\Omega_2$ over ϕ_r and ϕ_1, they could be influenced by the choice of bin size. In Fig. 20(e), the ratio of the $d^2\sigma/d\theta_1 d\theta_2$ cross sections computed with $\Delta\phi_r$ equal to 0.2 and 0.1 is shown. With the exception of one point ($\theta_S = 44°$, $\theta_D = 8°$), the change was always smaller than 2.5%.

6. Influence of theoretical weights

Since the correction factor used in the calculation of the cross sections depended on a specific theoretical model, the cross sections must be influenced to some extent by the particular choice of model. To understand the extent of this dependence, the experimental cross sections were also calculated assuming that the cross sections were determined by the phase space factor alone.[45] The results in Fig. 20(f) show that the differences between the two sets of data are smaller than 3% in all cases except one.

At the level of the $d^2\sigma$ and $d^3\sigma$ cross sections, the variation in the ratio of the cross sections is much greater, the maximum being ~±20%, although 2–8% is typical. In this context two points should be noted. The first is that the largest variations occur in the tails of the ϕ_r distributions where the phase space correction factors are systematically lower than the corresponding H-J correction factors. The second point is that phase space gives a very poor approximation to the expected theoretical distributions in ψ_γ and ϕ_r. For example, it will not reproduce the expected quadrupole shape in the ψ_γ distributions. The basic conclusion which can be drawn from this is that for an accurate interpretation of the experimental results, it is necessary to include some model dependence in the correction factors. However, assuming that the model reproduces the gross features of the experimental distributions, the particular choice does not appear to be critical.

7. Harvard and spherical polar coordinates

The theoretical cross sections used for comparison with the experimental results are expressed in terms of Harvard coordinates ($\bar{\theta}_1, \bar{\theta}_2, \bar{\phi}_r, \psi_\gamma$) while, for historical reasons, the experimental cross sections were expressed in terms of spherical polar coordinates ($\theta_1, \theta_2, \phi_r, \psi_\gamma$). Since ψ_γ is identical in both coordinate systems and ϕ_r is very nearly equal to $\bar{\phi}_r$, the only significant variation comes with respect to the polar angles. This is shown in Fig. 20(g) where $(d^2\sigma/d\bar{\theta}_1 d\bar{\theta}_2)/(d^2\sigma/d\theta_1 d\theta_2)$ (theoretical) is plotted as a function of θ_S for different values of θ_D. The ratio varies from 1.038 at $\theta_D = 0°$, $\theta_S = 36°$ to 0.967 for $\theta_D = 8°$, $\theta_S = 68°$. Because the variation within a given polar angle bin is negligible, this ratio can be regarded as a correction factor which can be applied uniformly to all levels of cross sections in a given polar angle bin.

For the results presented in this paper, the $d^2\sigma$ cross sections have been corrected for this. Because of the magnitude of the statistical errors, the $d^2\sigma$ and $d^3\sigma$ cross sections have not been corrected.

E. Interpretation of results

At the level of the $d^3\sigma/d\Omega_1 d\Omega_2 d\psi_\gamma$ cross sections, there is some disagreement between experiment and theory; that is, between $\sigma^{\mathrm{EXP}}(\vec{q}_0)$ and $\sigma^{\mathrm{SIM}}(\vec{q}_0)$, but the error bars are in general too large to draw any firm conclusions. For some $d^2\sigma/d\Omega_1 d\Omega_2$ cross sections, (e.g., 30°–30° and 26°–30°) the agreement is excellent, while for others (e.g., 22°–26° and 26°–38°) the discrepancy is quite strong (see Fig. 18 and Ref. 9).

At the level of the $d^2\sigma/d\theta_1 d\theta_2$ cross sections, for large values of θ_S and small values of θ_D, the agreement between the theory and experiment is quite good. However, as θ_S decreases, $\sigma^{\mathrm{EXP}}(\vec{q}_0)$ becomes distinctly smaller than $\sigma^{\mathrm{SIM}}(\vec{q}_0)$. In this context, it is interesting to note that, for symmetric data ($\theta_D = 0$), the McGill results show the same trend in behavior, and that the Orsay data forms a natural extrapolation of the data reported here to lower values of θ_S, even though both these experiments were done at distinctly higher energies.

Since the OFES effects are expected to become more pronounced at smaller values of θ_S, this appears to indicate that the H-J potential may not be able to provide a good description of OFES effects. The second major trend apparent in the data is the increasing discrepancy between $\sigma^{\mathrm{EXP}}(\vec{q}_0)$ and $\sigma^{\mathrm{SIM}}(\vec{q}_0)$ with increasing θ_D, a feature which is also corroborated by the Orsay data. At present, there does not appear to be an adequate interpretation of this effect.

The influence of systematic effects on the data was discussed in the previous section. While, in some cases, the effect on the data was not negligible when compared with the statistical errors, the general tendency was to increase the discrepancy between $\sigma^{\mathrm{EXP}}(\vec{q}_0)$ and $\sigma^{\mathrm{SIM}}(\vec{q}_0)$ rather than to decrease it. In any case, it was found that no reasonable assumptions about the magnitude of the systematic effects were able to produce shifts large enough to bring the theory and experiment into agreement. In this context, the data at $\theta_S = 48°$, $\theta_D = 4°$ should be emphasized. The experimental data here show strong disagreement with theory, particularly in the coplanar regions. Yet as can be seen from Fig. 20, systematic effects have very little influence on this data point and the statistics are quite good.

In summary, at the level of the $d^2\sigma/d\theta_1 d\theta_2$ cross sections, a significant disagreement is observed between the experimental results and the predictions of a model based on the H-J potential. Due to the restrictive nature of the conventional analysis, it is not possible to investigate this disagreement in more detail. This is done in the next section.

IX. GLOBAL ANALYSIS AND RESULTS

The global analysis is a procedure for comparing the results of an experiment with a theoretical calculation in a manner which bypasses the approximations needed in solving Eq. (3). Furthermore, it allows easy grouping of data in arbitrary parts of phase space, thus increasing, in a readily apparent form, their statistical significance. An outline of this procedure was presented in Sec. II. The most important results from the global analysis have been presented previously (cf. L3 and Ref. 9). In this section, some additional comments on the procedure and a detailed description of the results are presented.

A. Procedure

The theoretically weighted set of simulated events described in Sec. IV formed the starting point of the global analysis. Following the discussion in Sec. VIII A [see Eqs. (10)–(13)], the ratio of the number of ppB events detected in the range $\Delta\vec{q}$ to the number of simulated events that would be detected by the spectrometer in the same range can be written

$$R(\vec{q}_0) \equiv \frac{\Delta N^{\mathrm{ppB}}(\vec{q}_0)}{\Delta N^{\mathrm{HIT}}(\vec{q}_0)} = \frac{\alpha(\vec{q}_0)\sigma^{\mathrm{EXP}}(\vec{q}_0)}{\alpha^*(\vec{q}_0)\sigma^{\mathrm{SIM}}(\vec{q}_0)} . \tag{26}$$

Recalling that $\alpha(\vec{q}_0)$ and $\alpha^*(\vec{q}_0)$ describe the detection efficiency of the spectrometer for experimental events and those generated according to the theoretical model in question, it follows that if $\sigma^{\mathrm{SIM}}(\vec{q}\,') = \sigma^{\mathrm{EXP}}(\vec{q}\,')$, then $\alpha^*(\vec{q}_0) = \alpha(\vec{q}_0)$. In other words, if the model used to generate the simulated events adequately describes the ppB process, then $R(\vec{q}_0) = 1$. However, if $\sigma^{\mathrm{SIM}}(\vec{q}\,') \neq \sigma^{\mathrm{EXP}}(\vec{q}\,')$, then $\alpha^*(\vec{q}_0)$ and $\alpha(\vec{q}_0)$ describe how these different distributions propagate through the spectrometer. In this case, $R(\vec{q}_0)$ will no longer be equal to one and the variations in $R(\vec{q}_0)$ will be directly related to the differences between $\sigma^{\mathrm{SIM}}(\vec{q}\,')$ and $\sigma^{\mathrm{EXP}}(\vec{q}\,')$. Thus, $R(\vec{q}_0)$ provides a direct experimental test of the validity of the theoretical model under consideration. Unlike the conventional analysis, there is never any need to assume $\alpha^*(\vec{q}_0) = \alpha(\vec{q}_0)$ and, thus, bias the results in favor of the model being tested.

This procedure assumes that the normalization of the simulated data is equivalent to that of the experimental data. The method used to normalize the simulated data is shown in Fig. 21(a). In the upper portion of the figure, the experimental and simulated distributions are shown as a function of θ_S. In addition to passing all ppB event selection criteria, these events have been restricted to the range $\theta_D < 2°$. The four points indicated by the joined arrows were used to normalize the simulated to the experimental data. These points were chosen because the results of the conventional analysis showed that, in this particular range, experiment and theory were in good agreement. This is reflected in the lower portion of the figure where the ratio of the two sets of data (experiment to theory) is plotted. In addition, the results from the top line ($\theta_D = 0°$) of Fig. 19 have been replotted here. These results represent a similar, but not identical, sample of events evaluated using the conventional analysis. The small difference between the two event samples arises from two causes: (1) in the conventional analysis, θ_L and θ_R were binned in 4° intervals while here all the data with $\theta_D < 2°$ were used; (2) the conventional results were based on the first analysis of the data while the global results are based on the reanalyzed data. Keeping these differences in mind, the agreement between the two results is good, thus demonstrating the consistency of the conventional and global methods.

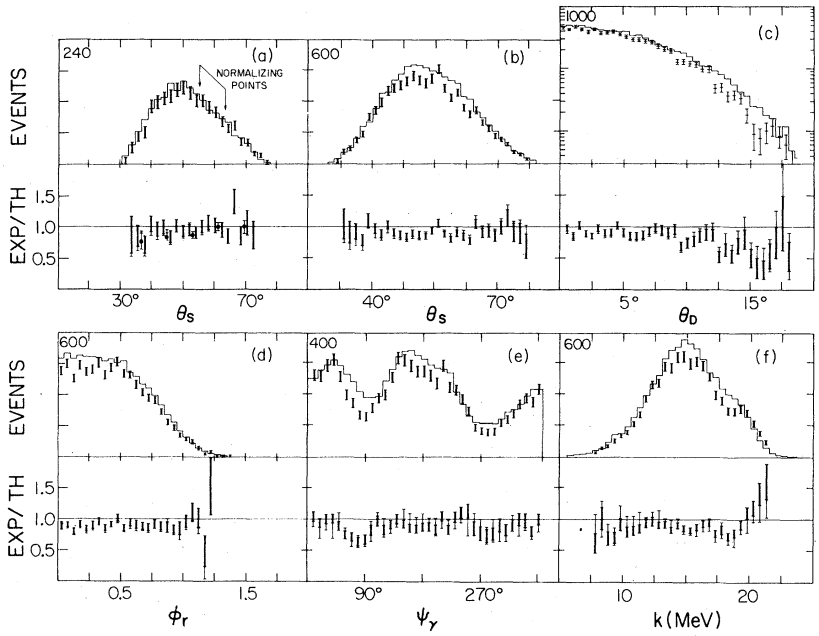

FIG. 21. In the top and bottom half of each panel, the distribution of all experimentally detected events (points with error bars), the corresponding simulated events (histograms) and their ratios are shown as a function of the variable indicated below the panel (see Appendix I for the definition of variables). The heavy error bars are due to statistical errors only. The extended light bars in the ratios show possible systematic effects due to the uncertainty in the energy calibration of the scintillation counters (see Sec. V A). See text for explanation of joined arrows and full circles in panel (a). The numbers in the upper left hand corner correspond to the number of events at the top (fourth) scale marker.

B. Experiment to theory comparison

All of the global results presented in this paper, as well as those in L3 and Ref. 9, are based on the reanalyzed data from Exp. II.

The simplest and statistically most significant experiment to theory comparison was made by integrating the data over all variables except one. The advantage of the global procedure in this case is that the analysis can be easily made in terms of any variable, regardless of whether or not it was measured explicitly. Some results are shown in Figs. 21 and 22.

Comparing experiment with theory in terms of multiple differential cross sections has the obvious advantage of emphasizing details which might be otherwise masked. Unfortunately, the resulting increase in the number of bins leads to a smaller number of events per bin, and often makes the interpretation of the results statistically inconclusive. Using the global method, it is easy to achieve a balance between loss of detail due to coarse binning, and integration, and poor statistics caused by choosing too many bins.

Some results of the global analysis, in terms of multiple differential cross sections, are shown in Figs. 23–26. In each case, the numbers in the upper left hand corner correspond to the number of events at the top (fourth) scale marker.

C. Calculation of cross sections and matrix elements

In Fig. 27, a series of partially integrated (nonrandomized) $d^5\sigma/d\theta_S' d\theta_D' d\phi_r' d\phi_1' d\psi_\gamma'$ cross sections is presented in relative units. These cross sections are defined as follows:

$$\frac{d\sigma(\psi_\gamma')}{d\psi_\gamma'} = \int_{\theta_{S1}'}^{\theta_{S2}'} d\theta_S' \int_{\theta_{D1}'}^{\theta_{D2}'} d\theta_D' \int_{\phi_{r1}'}^{\phi_{r2}'} d\phi_r' \int_{\phi_{11}'}^{\phi_{12}'} d\phi_1' \times \frac{d^5\sigma}{d\theta_S' \, d\theta_D' \, d\phi_r' d\phi_1' d\psi_\gamma'} \,. \tag{27}$$

A comparison of the results in Figs. 24 and 27 provides a semiquantitative correlation between the global results and the theoretical cross sections. Since the regions A–D in Fig. 2, which correspond to the ranges of integration in Fig. 24, are larger than those covered in Fig. 27, it is reasonable to assume that where the global method shows good agreement between experiment and theory, the theoretical cross sections provide an adequate description of the ppB process. Where the global method shows disagreement, this disagreement can be used to estimate the change

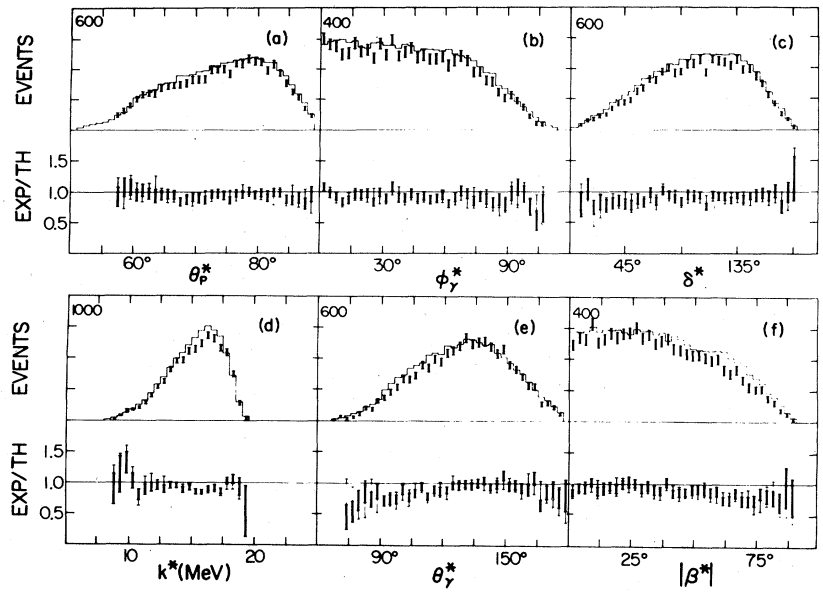

FIG. 22. The distributions and ratios are as described in Fig. 21, but are expressed as a function of some variables in the c.m. system.

necessary to bring the theoretical cross sections into agreement with experiment. This is indicated by the dashed lines in Fig. 27.

The simulated data were also used to examine the behavior of the matrix elements. The mean value of the square of the matrix element was evaluated as a function of the photon energy using the following expression:

$$|M(k')|^2 = \frac{\int_{\theta'_{S1}}^{\theta'_{S2}} d\theta'_S \int_{\theta'_{D1}}^{\theta'_{D2}} d\theta'_D \int_{\phi'_{r1}}^{\phi'_{r2}} d\phi'_r \int_{\phi'_{11}}^{\phi'_{12}} d\phi'_1 |M(k', \theta'_S, \theta'_D, \phi'_r)|^2 F(k', \theta'_S, \theta'_D, \phi'_r)}{\int_{\theta'_{S1}}^{\theta'_{S2}} d\theta'_S \int_{\theta'_{D1}}^{\theta'_{D2}} d\theta'_D \int_{\phi'_{r1}}^{\phi'_{r2}} d\phi'_r \int_{\phi'_{11}}^{\phi'_{12}} d\phi'_1 F(k', \theta'_S, \theta'_D, \phi'_r)}, \tag{28}$$

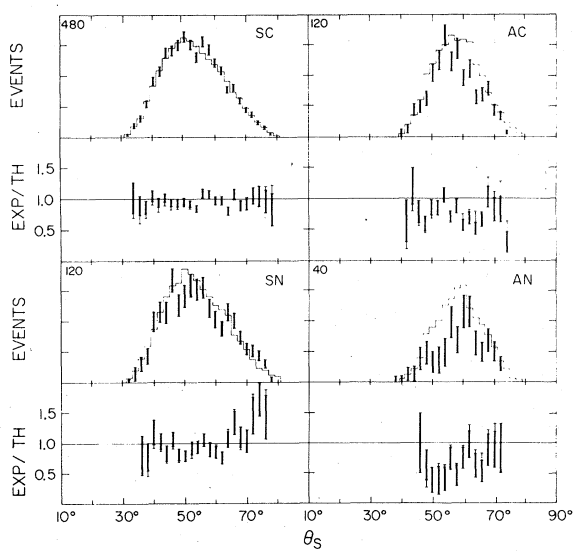

FIG. 23. The distributions of the detected and simulated events and their ratios are shown as a function of θ_S subject to the constraints $S(0° \leq \theta_D < 9°)$, $A(9° \leq \theta_D < 20°)$, $C(0 \leq \phi_r < 0.7)$, and $N(0.7 \leq \phi_r < 1.4)$ as indicated in the drawing.

where $F(k', \theta'_S, \theta'_D, \phi'_r)$ is the phase space density factor and the ranges of integration are the same as described for Fig. 27.

In Fig. 28, histograms of $|M(k')|^2$ are plotted on a log-log scale as a function of the photon energy in the laboratory system. A comparison between Figs. 25 and 28 again provides a means to estimate the experimental value of the squares of the matrix elements. As in Fig. 27, a dashed line is used to indicate the inferred experimental values where disagreement exists.

D. Systematic errors

Some of the systematic effects, such as binning, influence of the theoretical weights, and the approximations used in Eq. (16), which are important in conventional analysis, become completely irrelevant in the global analysis. Other effects which might influence the results are discussed in this section.

1. Prompt background subtraction

The only additional treatment of the prompt background in the global analysis was to remove any

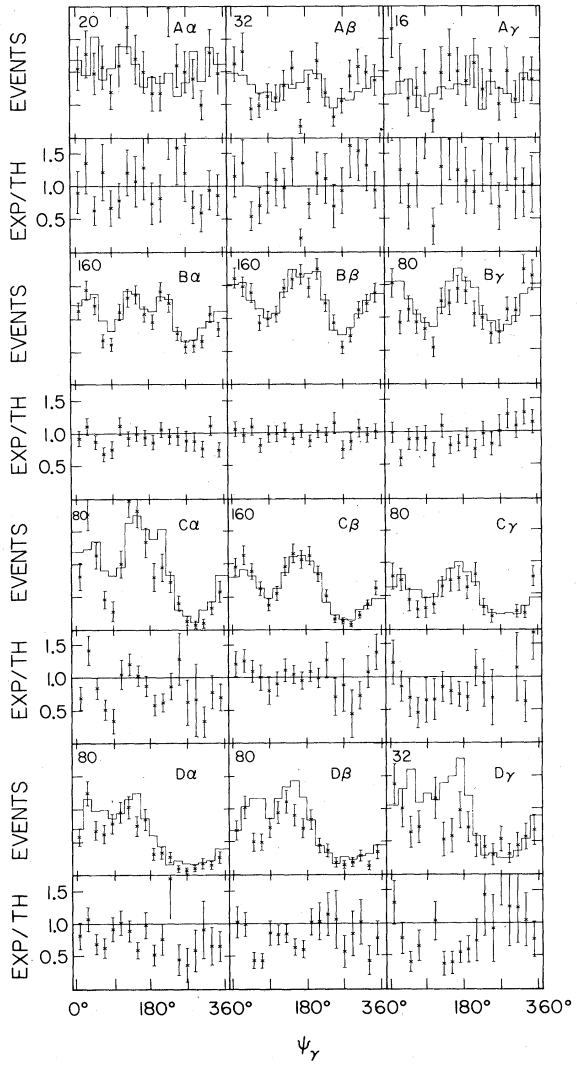

FIG. 24. The distributions of the detected and simulated events and their ratios are shown as a function of the Harvard photon angle ψ_γ for the four regions A, B, C, and D outlined in Fig. 2, and three ranges of relative noncoplanarity $\alpha(0 \leq \phi_r < 0.3)$, $\beta(0.35 \leq \phi_r < 0.65)$, and $\gamma(0.7 \leq \phi_r < 1.4)$.

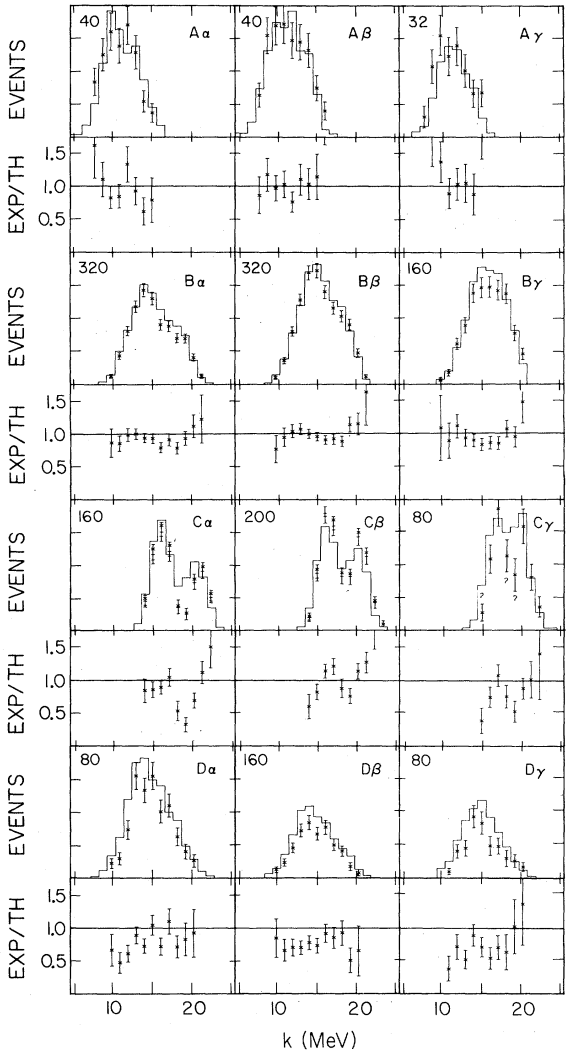

FIG. 25. The distributions are as described in Fig. 24, but are expressed as a function of lab photon energy k.

point in which the prompt background correction constituted more than 25% of the total number of prompt events. Where there was a marked discrepancy between experiment and theory, the data were checked to see if this could have been caused by an overestimation of prompt background. In the regions of largest discrepancy, it was found that even if no prompt background were subtracted, the discrepancies would still exist. Since it was more probable that the prompt background was underestimated rather than overestimated (see Sec. VI C 5) it is more likely that the disagreements between experiment and theory are larger than those depicted.

2. *Angular asymmetry test*

It has been shown in both the conventional and global analyses [see Figs. 19 and 21(c)], that a significant discrepancy between experiment and theory exists for large values of θ_D. Because this effect occurs in a region of the spectrometer where the detection efficiency decreases rapidly, it was important to ensure that it did not arise from any possible undetected experimental asymmetries. This possibility was studied and the results are shown in Fig. 29. In parts (a) and (b), symmetric geometric constraints have been imposed on the

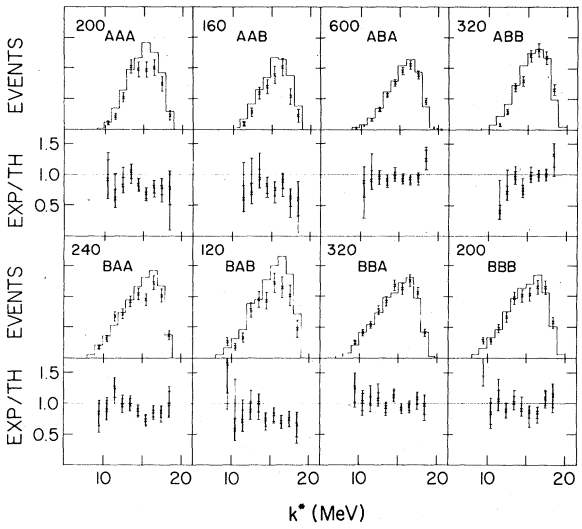

FIG. 26. The distributions of the detected and simulated events and their ratios are shown as a function of k^*, the photon energy in the c.m. system subject to the following constraints as indicated on the drawings. The first letter signifies that either $\theta_p^* < 75°$ (A) or $\theta_p^* \geq 75°$ (B). Similarly, the second letter signifies that either $\theta_\gamma^* < 120°$ (A) or $\theta_\gamma^* \geq 120°$ (B) and the third that either $\phi_\gamma^* < 50°$ (A) or $\phi_\gamma^* \geq 50°$ (B).

data so that both the experimental and simulated distributions should be symmetric about $\theta_L - \theta_R = 0°$. If just the heavy error bars are considered in the EXP/TH ratio, then, within statistics, the

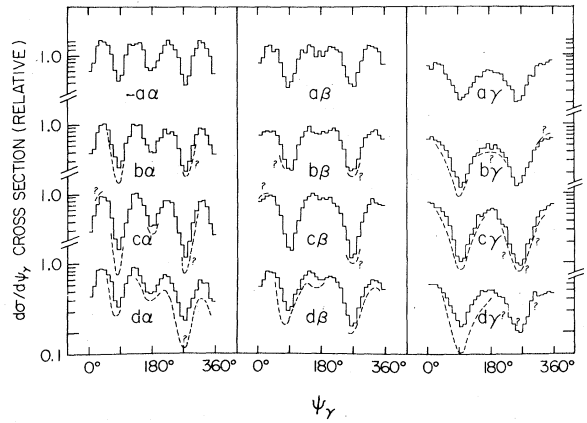

FIG. 27. The $d\sigma/d\psi_\gamma'$ cross sections as defined by Eq. (27) are plotted for the four shaded regions, a ($66° \leq \theta_S' < 78°$ and $\theta_D' < 2°$), b ($46° \leq \theta_S' < 58°$ and $\theta_D' < 4°$), c ($32° \leq \theta_S' < 44°$ and $\theta_D' < 4°$), and d ($46° \leq \theta_S' < 58°$ and $9° < \theta_D' < 13°$) shown in Fig. 2 and for three different ranges of the relative noncoplanarity α ($\phi_\gamma' < 0.3$), β ($0.35 \leq \phi_\gamma' < 0.65$), and γ ($0.7 \leq \phi_\gamma' \leq 1.0$) as a function of the photon angle ψ_γ'. The dashed curves indicate the regions and the approximate size of the disagreements between experiment and theory. The question marks placed near certain portions of the curves indicate that disagreement is only suggestive.

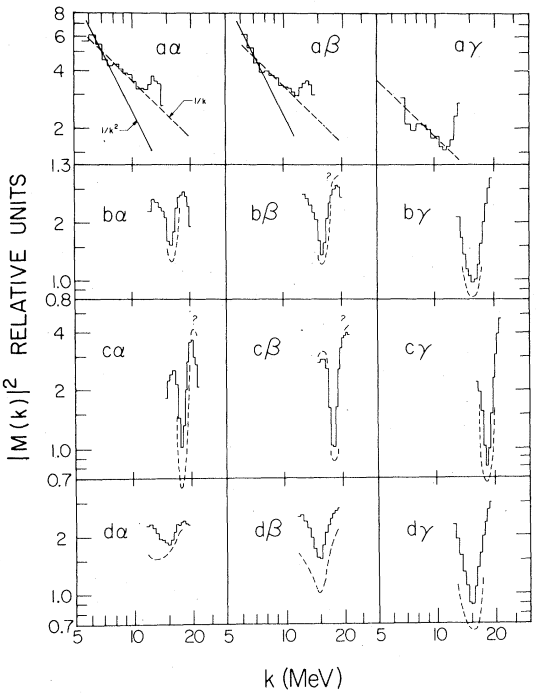

FIG. 28. The squares of the matrix elements as defined by Eq. (28) are plotted as a function of photon energy k' for the same phase space regions as in Fig. 27. The meaning of the dotted curves and the adjacent question marks is the same as in Fig. 27. The heavy and dashed lines in the top three panels correspond to a $1/k'^2$ and $1/k'$ dependence, respectively, as is expected from the first and the first two terms of the soft photon approximation, respectively.

data show a satisfactory degree of symmetry. The effect of extending the error bars to allow for the uncertainty in the energy calibration is to *decrease* this symmetry. This gives additional evidence that the energy calibration used was the best choice. In Figs. 29(c) and (d), the data have been selected so that differences between the proton polar angles are maximized. The EXP/TH ratio shows a large discrepancy for large $\theta_L - \theta_R$ which is decreased when the error bars are extended. In other words, the most accurate energy calibration is that which also produces the largest disagreement between experiment and theory.

3. *Low energy events*

From the discussion in Sec. V A and Fig. 9, it follows that the energy calibration curves are least reliable at very low detected energies. One region where experiment and theory disagree strongly is at asymmetric angles, where one of the protons has a rather small energy. Because of this, it was important to check whether or not this disagreement was based solely on these low energy events.

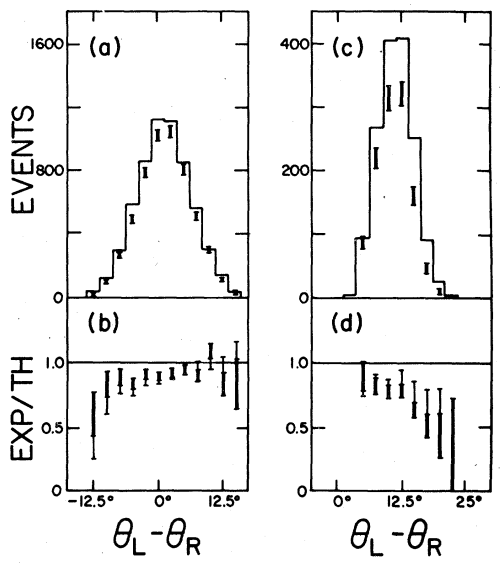

FIG. 29. The distributions of the detected and simulated events and their ratios are shown as a function of the difference in the detected proton polar angles $\theta_L - \theta_R$. In parts (a) and (b), the constraints applied were "symmetrized" by requiring that the horizontal wire chamber coordinates have the same (i.e., symmetrical) ranges in both the left and right spectrometer arms. In parts (c) and (d), the constraints were "antisymmetrized" by requiring that the horizontal wire chamber coordinates have nonoverlapping (i.e., entirely asymmetrical) ranges in the two arms.

There also existed the possibility that unknown errors in the positioning of the low energy cutoffs could produce this type of discrepancy. To test for these possibilities, the results presented in Fig. 23 were redetermined with the cutoffs set at 7.5 MeV (detected energy) in both the experimental and simulated data (see Sec. SIV) for details). The modified EXP/TH ratios are shown in Fig. 30.

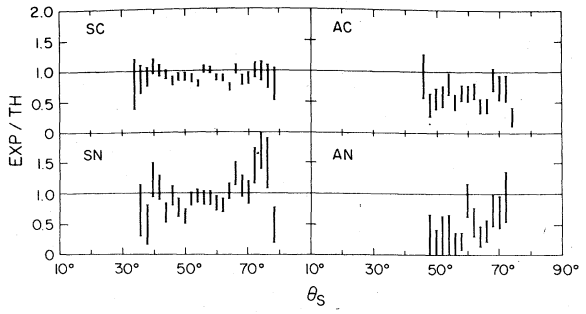

FIG. 30. The ratios of the detected and simulated events are plotted as a function of the sum of the proton angles θ_S subject to the same combination of constraints as in Fig. 23 except that the detected energies in both scintillation counters were constrainted to be larger then 7.5 MeV.

In parts (*SC*) and (*SN*), which correspond to events with $\theta_D < 9°$, very little change is evident between Figs. 23 and 30. In parts (*AC*) and (*AN*), where results are presented for events with $\theta_D > 9°$, a comparison between Figs. 23 and 30 shows that the EXP/TH ratio in Fig. 30 is suppressed even more than in Fig. 23, particularly for small θ_S. Because of the relatively poor statistics, this additional suppression is not regarded as being significant, but the results certainly establish that the observed discrepancy is not caused solely by the very low energy events. The error bar extensions due to the uncertainty in the energy calibration have not been included in Fig. 30 because, above 7.5 MeV, the differences in the calibrations are relatively minor.

4. *Angular resolution*

As pointed out in Sec. IV A and discussed in Sec. SV A, an error in the simulation program resulted in the overestimation of the angular resolution. The major effect of this was to alter the simulated distribution in ϕ_r. Consequently, any results in which ϕ_r was not completely integrated over were distorted. To compensate for this, a correction procedure, described in Sec. SV A, was developed and applied to the data. Specifically, this affected the results presented in Figs. 21(d), 23, and 30. Note that the result in Fig. 23 (*AN*) is different from that in L3, where this correction was not applied.

E. Interpretation of results

The results presented in Sec. IX B indicate that, in certain regions of phase space, there is a significant discrepancy between experiment and theory. Cases for which the EXP/TH ratio differs from one by $\lesssim 10\%$ are not regarded as significant because of the uncertainties associated with the normalization procedure. Several factors contributed to this uncertainty. First, in normalizing the global results to the conventional ones, the sample of data used had a statistical error of ~5%. Secondly, the normalization of the conventional data was only accurate to 4% (see Table V in Sec. VII). Finally, although in the first analysis the global and conventional results agreed to within 1% in the range used for normalization, this increased to 4% when the data were reanalyzed. As a result, the normalizing error in all global results is estimated to be ~6–8%.

In Fig. 21(e), there exists a marked discrepancy around $\psi = 80°$. This is precisely the point where studies by Fearing[46] show that the first term in Low's low energy expansion (*A*, in Fearing's notation) is equal to zero. This discrepancy in-

creases as θ_S decreases, becoming almost a factor of three for the smallest values of θ_S (see panel $C\alpha$ in Fig. 24). For events with symmetric polar angles, the behavior must be reflected at $\psi_\gamma = 280°$ while, for asymmetric events, this is not necessarily so. The data also show some discrepancy at $\psi_\gamma = 280°$, but it is not as conclusive as it is at 80°.

The disagreement between experiment and theory increases strongly with increasing θ_D [see Fig. 21(c)]. The origin of this behavior is not understood.

The discrepancies do not increase monotonically with photon energy. In this context, it should be noted that the regions of disagreement in Figs. 24 and 25 are kinematically correlated. For the ranges of θ_S and θ_D under consideration, $\psi_\gamma = 80°$ corresponds to intermediate values of the photon energy.

The disagreements occur predominantly where the cross sections are small. In Fig. 27, where the cross sections are shown on a relative scale of 0.1 to 2.5, the most significant discrepancies occur when the (relative) cross sections are less than about 0.3 to 0.4. This can again be correlated with the fact, as Fearing found, that $A = 0$ in these regions.

In panel AN of Fig. 23 (corresponding to asymmetric, noncoplanar events), a very strong disagreement between experiment and theory is demonstrated. When all of the events in the panel are summed, the EXP/TH ratio is 0.63 ± 0.06.[47] These same events are shown in panel $D\gamma$ of Figs. 24 and 25 in different form, while the shapes of the corresponding cross sections and matrix elements are shown in panel $d\gamma$ of Figs. 27 and 28, respectively. From Figs. 24 and 25, it can be seen that this disagreement spans a range of from 60° to 200° in ψ_γ and, except for the very highest energies, covers the full range of kinematically allowed photon energies.

Finally, some comments can be made concerning the matrix elements shown in Fig. 28. It is evident that in region a, for photon energies between 7 and 11 MeV, the matrix elements have a $1/k$ dependence; at energies smaller than 7 MeV, the results are inconclusive but are consistent with a $1/k^2$ dependence setting in. At energies above about 11 MeV, the shape of the curves[48] becomes anything but proportional to $1/k$ or $1/k^2$. It is difficult to draw firm conclusions from these curves, but they do suggest that for photon energies above about 10 MeV, Low's low energy theorem is not applicable which would, in turn, imply that the off-energy-shell contributions to the cross sections (or matrix elements) might not be negligible.

X. CONCLUSIONS

At the time of the execution of this experiment, no previous bremsstrahlung experiment had utilized the wire chamber and on-line computer technology needed to attain the data-taking rates for a high statistics experiment. This experiment demonstrated that it was practical to use such an approach at relatively low incident energies, the benefits being improved angular resolution and two orders of magnitude increase in the ppB event rate.

The results of this experiment are in significant disagreement with a theoretical calculation based on the Hamada-Johnston potential. This discrepancy is most apparent at large values of θ_D, large noncoplanarities, and for $\psi_\gamma \approx 80°$. It is relevant to note that the latter corresponds to a region where the cross sections are relatively small, not where the photon energy is large. The pattern of disagreement is similar to that observed in the Orsay experiment.[44] The reasons for the disagreement are not understood at present, but may indicate that the Hamada-Johnston potential is not adequate to describe OFES effects.

The evidence for this disagreement, although highly suggestive, cannot be regarded as conclusive at this time. The reason for this is twofold. First, all known corrections have not been included in the theoretical calculation.[49] Second, the experiment was subject to certain systematic errors, the most significant of which was the uncertainty in the energy calibration at detected energies $\lesssim 8$ MeV. Through the use of the global procedure, it was established that no single source of systematic error was large enough to produce the observed disagreement. However, it is conceivable that a "conspiracy" of systematic effects and approximations made in the theoretical calculation are responsible for this disagreement. Therefore, the experiment and analysis reported here should be regarded as providing strong, but not necessarily conclusive, evidence that the H-J potential is inadequate to describe the details of the pp bremsstrahlung process at 42 MeV.

ACKNOWLEDGMENTS

Because of the long duration of this project, many people contributed to it in varying degrees. We wish to thank Dr. K. G. Standing and Dr. J. S. C. McKee for providing general support and, in the case of Dr. Standing, contributions made in the early stages of the experiment. Mr. D. Reimer, Mr. R. Kawchuck, Dr. R. King, and Dr. E. Lipson and, especially, Mr. P. O'Connor developed much of the software used in this experiment. Mr. T. W. Millar and Mr. D. G. Peter-

son were responsible for the development of much of the software and hardware used for the scintillation counters and the beam positioning device, respectively. Dr. J. C. Thompson and Dr. J. McKeown were instrumental in the development of the wire chamber spectrometer. Dr. W. F. Prickett, Dr. K. F. Suen, and Dr. R. Kerchner each made significant contributions to this experiment. Special thanks are due to Dr. M. K. Liou for allowing us to use his computer code for the calculation of the theoretical cross sections. The able assistance of Mr. G. Knote and Mr. A. Neufeld during the manufacture of the wire chambers and some associated electronics is gratefully acknowledged. The technical support of the cyclotron staff during the execution of this experiment and the cooperation of Mr. D. Reimer, Mr. J. Epp, Mr. H. Nottelman, and other personnel of the University of Manitoba Computer Center during the analysis stages of this experiment are gratefully acknowledged.

This work was supported by the Atomic Energy Control Board, National Research Council of Canada, and the Research Board of the University of Manitoba.

APPENDIX A: DEFINITION OF VARIABLES AND COORDINATE SYSTEMS

1. Laboratory system

Three different laboratory coordinate systems are used in this paper.

The *spectrometer coordinate system* is used to define the experimentally determined quantities. The cartesian and spherical polar coordinates of a ppB event in this system are shown in Fig. 31. The beam is assumed to be moving in the $+Z$ direction and the X axis is horizontal. A proton moving to the left in the X-Z plane has $\phi_L = 0$. The relative noncoplanarity, ϕ_r is defined through the relation

$$\phi_r = |\phi_D|/\phi_{DM}, \tag{A1}$$

where $\phi_D = \phi_R - \phi_L - \pi$ is the event noncoplanarity and ϕ_{DM} is the maximum value of ϕ_D allowed by kinematics. With this definition, ϕ_D and, hence, ϕ_r are zero for coplanar events. The advantage of using ϕ_r is that, since ϕ_{DM} is a function of θ_L and θ_R as well as the incident energy, it provides a means to compare data taken at different angles and energies.

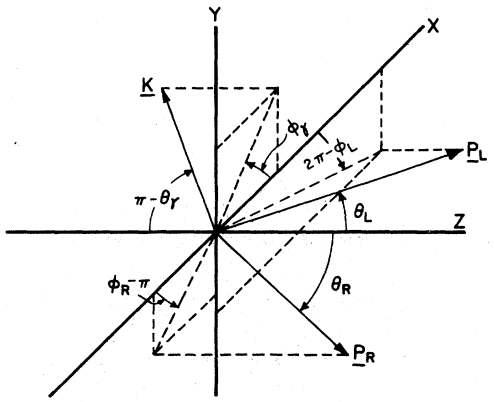

FIG. 31. Schematic diagram of a noncoplanar ppB event in the spherical polar coordinate system. P_L, P_R, and K denote the momentum vectors of the left and right protons and the photon, respectively.

The identity of the two final state protons and the existence of axial symmetry makes any distinction between left and right irrelevant from the theoretical point of view. For this reason, an *event coordinate system* (using spherical polar coordinates) was defined such that the proton characterized by the smaller of the two polar angles, θ_L and θ_R, (designated particle 1) was specified to have $\phi = 0$. The remaining proton was designated particle 2. Thus, the event coordinate system and the spectrometer coordinate system were related through a rotation about the z axis by an amount ϕ_L or ϕ_R, this being different for each event. The variables ϕ_D and ϕ_r are identical in either system. Note that because the polar angles were calculated by the computer to many significant digits, for all practical purposes the case where θ_L and θ_R were identical never arose. One could always make the choice of a smaller angle.

For reasons of convenience, the theoretical calculations were performed in the *Harvard coordinate system* (see Fig. 32) where the angles for the protons are $\overline{\theta}_L$, $\overline{\theta}_R$, $\overline{\phi}_L$, and $\overline{\phi}_R$ (cf. Ref. 28 and T4). These angles are defined by projecting the proton momenta onto the X-Z plane. $\overline{\theta}_L$ and $\overline{\theta}_R$ are the angles between these projections and the Z axis while $\overline{\phi}_L$ and $\overline{\phi}_R$ are the angles that the proton momenta make with these projections onto the X-Z plane. The angle $\overline{\phi} = (\overline{\phi}_L + \overline{\phi}_R)/2$ has a maximum kinematically allowed limit, $\overline{\phi}_M$. If the orientation of the X-Z plane is chosen such that $\overline{\phi}_L = \overline{\phi}_R$, then the event noncoplanarity is given by $\overline{\phi} = \overline{\phi}_L = \overline{\phi}_R$ and the relative noncoplanarity by

$$\overline{\phi}_r = \overline{\phi}/\overline{\phi}_M . \tag{A2}$$

Within the range of angles observed in this experiment, ϕ_r and $\overline{\phi}_r$ are very nearly equal so that it makes no practical difference whether the cross sections are expressed as a function of ϕ_r or $\overline{\phi}_r$.

A major problem arises[28] when one tries to present bremsstrahlung differential cross sections in terms of the photon polar angle θ_γ (or $\overline{\theta}_\gamma$). For

noncoplanar events, this angle does not span the full range from 0 to π, and kinematic singularities exist at the end points. Also, for asymmetric events, θ_γ alone cannot distinguish whether the photon is on the side of particle 1 or particle 2. For these reasons, a projected photon angle which spans the full range from 0 to 2π was defined in the following manner (see Fig. 32):

(1) for a given $\bar{\theta}$ (or θ) pair, the limiting photon momentum $\vec{K}_0$ (i.e., at maximum noncoplanarity) is determined;

(2) the reaction plane is oriented so that $\phi_L = \phi_R$;

(3) a plane X'-Z' is constructed parallel to the X-Z plane passing through the tip of $\vec{K}_0$;

(4) the photon momentum $\vec{K}$ is multiplied by a constant α such that the point of $\alpha\vec{K}$ meets the X'-Z' plane;

(5) ψ_γ is defined as the angle between the beam direction and $\alpha\vec{K} - \vec{K}_0$.

The range of ψ_γ is thus from 0 to 2π. The convention used in this paper is that the range $0 < \psi_\gamma < \pi$ always corresponds to the case where the photon is on the same side of the beam as particle 1. If one considers a ppB ellipse in the E_1-E_2 plane, where E_1 is plotted along the abscissa, ψ_γ always increases in a clockwise direction. (Note that with this convention, in the *event* coordinate system, the center of the ppB ellipse always lies below the line $E_1 = E_2$.)

For convenience, the formulas relating the spherical and Harvard angles are included below.

$$\psi_\gamma = \tan^{-1}\frac{\sin\bar{\theta}_\gamma - \cot\bar{\phi}_0 \tan\bar{\phi}_\gamma \sin\bar{\theta}_0}{\cos\bar{\theta}_\gamma - \cot\phi_0 \tan\phi_\gamma \cos\bar{\theta}_0}$$

$$= \tan^{-1}\frac{\sin\theta_\gamma \cos\phi_\gamma - \sin\theta_\gamma \cot\phi_0 \sin\phi_\gamma}{\cos\theta_\gamma - \sin\theta_\gamma \sin\phi_\gamma \cot\theta_0 \csc\phi_0}\,, \quad \text{(A3)}$$

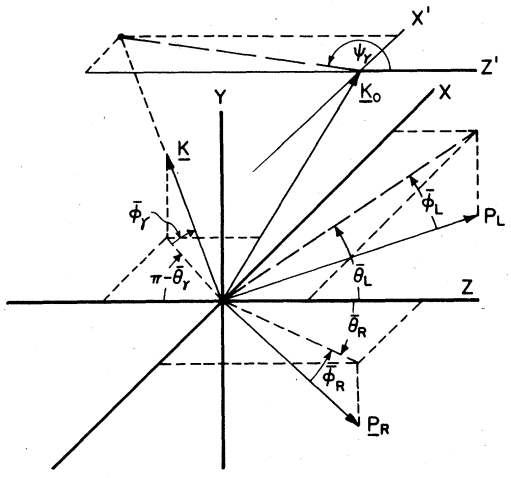

FIG. 32. The same event depicted in Fig. 31 shown in the Harvard coordinate system. K_0 is the photon momentum in the limiting kinematic case.

$$\phi = \tan^{-1}(\csc\bar{\theta}_i \tan\bar{\phi})\,, \quad \text{(A4)}$$

$$\Theta_i = \tan^{-1}(\tan^2\bar{\theta}_i + \sec^2\bar{\theta}_i \tan^2\bar{\phi})^{1/2}\,. \quad \text{(A5)}$$

In addition, two other laboratory variables, θ_S and θ_D, are commonly used in this paper. They are defined as follows:

$$\theta_S = \theta_L + \theta_R = \theta_1 + \theta_2\,, \quad \text{(A6)}$$

$$\theta_D = |\theta_L - \theta_R| = |\theta_1 - \theta_2|\,. \quad \text{(A7)}$$

2. Center of mass system

Two sets of variables were used to describe events in the center of mass system. In one case, the variables chosen were k^*, the photon energy, and the angular variables θ_p^*, δ^*, and β^*. θ_p^* is the smallest of the polar angles of the two protons defined with respect to either the positive or negative Z axis (i.e., the smallest of θ_L^*, θ_R^*, $180°-\theta_L^*$, or $180°-\theta_R^*$). δ^* is the angle between the proton characterized by θ_p^* and the photon and β^* is equal to $|\alpha^*-90°|$, where α^* is the angle between the normal to the reaction plane $(\vec{p}_1^* \times \vec{p}_2^*)$ and the Z axis. In the second case, k^* and θ_p^* were also used, but the angles δ^* and β^* were replaced by θ_γ^* and ϕ_γ^*. The definitions of these angles differ slightly from that of the conventional polar and azimuthal angles of the photon. θ_γ^* is the polar angle of the photon, but is measured from the same direction of the Z axis with respect to which θ_p^* was defined. ϕ_γ^* is given by the absolute value of the difference between the azimuthal angles of the proton characterized by θ_p^* and the photon.

APPENDIX B: DEFINITION OF CROSS SECTIONS

In bremsstrahlung experiments, the fivefold differential cross section is usually defined as

$$\frac{d^3\sigma}{d\Omega_1 d\Omega_2 d\psi_\gamma} = \frac{d^5\sigma(\theta_1, \theta_2, \phi_1, \phi_2, \psi_\gamma)}{d(\cos\theta_1)d(\cos\theta_2)d\phi_1 d\phi_2 d\psi_\gamma}\,. \quad \text{(B1)}$$

However, following the discussion in Appendix A, it is more convenient to express this cross section in terms of ϕ_1 (or ϕ_2) and ϕ_r than in ϕ_1 and ϕ_2. Noting that

$$d\phi_1 d\phi_2 = d\phi_1 d\phi_D = 2\phi_{DM} d\phi_1 d\phi_r\,, \quad \text{(B2)}$$

(the factor of 2 arises because ϕ_r is defined as the absolute value of ϕ_D divided by ϕ_{DM}) then we get

$$\frac{d^5\sigma(\theta_1, \theta_2, \phi_1, \phi_2, \psi_\gamma)}{d(\cos\theta_1)d(\cos\theta_2)d\phi_1 d\phi_2 d\psi_\gamma}$$

$$= \frac{1}{2\phi_{DM}} \frac{d^5\sigma(\theta_1, \theta_2, \phi_1, \phi_r, \psi_\gamma)}{d(\cos\theta_1)d(\cos\theta_2)d\phi_1 d\phi_r d\psi_\gamma}\,. \quad \text{(B3)}$$

For the case where both the beam and the target are unpolarized, the cross sections have rotation-

al symmetry about the beam axis and, hence, the angle ϕ_1 can be dropped from the list of arguments in Eq. (B3). This is the form of the cross section used in this paper.

To obtain the fourfold differential cross section, expression (B3) is integrated over ψ_γ from 0 to 2π. Thus,

$$\frac{d^2\sigma}{d\Omega_1 d\Omega_2} = \frac{d^4(\theta_1, \theta_2, \phi_\gamma)}{d(\cos\theta_1)d(\cos\theta_1)d\phi_1 d\phi_\gamma} = 2\phi_{DM}\int_0^{2\pi} \frac{d^5\sigma(\theta_1, \theta_2, \phi_\gamma, \psi_\gamma)}{d(\cos\theta_1)d(\cos\theta_2)d\phi_1 d\phi_\gamma d\psi_\gamma} d\psi_\gamma . \quad \text{(B4)}$$

The twice differential cross section is obtained by integration over ϕ_1 and ϕ_γ, so that

$$\frac{d^2\sigma(\theta_1, \theta_2)}{d\theta_1 d\theta_2} = 2\phi_{DM}\sin\theta_1 \sin\theta_2 \times \int_0^1 \int_0^\pi \frac{d^4(\theta_1, \theta_2, \phi)}{d(\cos\theta_1)d(\cos\theta_1)d\phi_1 d\phi_\gamma} \times d\phi_1 d\phi_\gamma . \quad \text{(B5)}$$

---

*Present address: Department of Physics, University of Alberta, Edmonton, Alberta T6G 2N5, Canada.

[1] P. Signell, Adv. Nucl. Phys. 2, 223 (1969).

[2] M. J. Moravcsik, Rep. Prog. Phys. 35, 587 (1972).

[3] M. K. Srivastava and Donald W. L. Sprung, Adv. Nucl. Phys. 8, 121 (1975).

[4] L. Heller, Bull. Am. Phys. Soc. 17, 480 (1972). See also P. Signell, in *Proceedings of the International Conference on Few Particle Problems in the Nuclear Interaction, Los Angeles, California, 1972*, edited by I. Slaus *et al.* (North-Holland, Amsterdam, 1973), pp. 1–25.

[5] G. E. Bohannon, *Nucleon-Nucleon Interactions, Proceedings of the Second International Conference on Nuclear-Nuclear Interactions, Vancouver, 1977,* edited by H. Fearing, D. Measday, and A. Strathdee (AIP, New York, 1978), pp. 482 and 494.

[6] M. Sobel and A. Cromer, Phys. Rev. 132, 2698 (1963).

[7] B. Gottschalk, W. Schlaer, and K. Wang, Phys. Lett. 16, 294 (1965); Nucl. Phys. 75, 549 (1966); A94, 491 (1967).

[8] M. L. Halbert, *Proceedings of the Gull Lake Symposium on the Two-Body Force in Nuclei*, edited by S. M. Austin and G. M. Crawley (Plenum, New York, 1972), p. 53.

[9] J. V. Jovanovich, *Nucleon-Nucleon Interactions, Proceedings of the Second International Conference on Nuclear-Nuclear Interactions, Vancouver, 1977,* edited by H. Fearing, D. Measday, and A. Strathdee (AIP, New York, 1978), p. 451.

[10] K. W. Rothe, P. F. M. Koehler, and E. H. Thorndike, Phys. Rev. Lett. 16, 1118 (1966); Phys. Rev. 157, 1247 (1967).

[11] J. V. Jovanovich, L. G. Greeniaus, J. McKeown, T. W. Millar, D. G. Peterson, W. F. Prickett, K. F. Suen, and J. C. Thompson, Phys. Rev. Lett. 26, 277 (1971) (henceforth referred to as L1).

[12] L. G. Greeniaus, J. V. Jovanovich, R. Kerchner, T. W. Millar, C. A. Smith, and K. F. Suen, Phys. Rev. Lett. 35, 696 (1975) (henceforth referred to as L2).

[13] J. V. Jovanovich, C. A. Smith, and L. G. Greeniaus, Phys. Rev. Lett. 37, 631 (1976) (henceforth referred to as L3).

[14] J. McKeown, L. G. Greeniaus, J. V. Jovanovich, W. F. Prickett, K. F. Suen, and J. C. Thompson, Nucl. Instrum. Methods 104, 413 (1972) (henceforth referred to as P1).

[15] J. McKeown, Nucl. Instrum. Methods 104, 433 (1972) (henceforth referred to as P2).

[16] L. G. Greeniaus, J. V. Jovanovich, J. McKeown, D. Reimer, and J. C. Thompson, Nucl. Instrum. Methods 104, 437 (1972) (henceforth referred to as P3).

[17] T. W. Millar and J. V. Jovanovich, Nucl. Instrum. Methods 104, 447 (1972) (henceforth referred to as P4).

[18] D. G. Peterson, Nucl. Instrum. Methods 104, 451 (1972) (henceforth referred to as P5).

[19] J. McKeown, Ph.D. thesis, University of Manitoba, 1970; also Manitoba Cyclotron Report No. 70-02 (unpublished) (henceforth referred to as T1).

[20] D. G. Peterson, M.Sci. thesis, University of Manitoba, 1970; also Manitoba Cyclotron Report No. 70-03 (unpublished) (henceforth referred to as T2).

[21] T. W. Millar, M.Sci. thesis, University of Manitoba, 1970; also Manitoba Cyclotron Report No. 70-07 (unpublished) (henceforth referred to as T3).

[22] L. G. Greeniaus, Ph.D. thesis, University of Manitoba, 1972 (unpublished) (henceforth referred to as T4); also Manitoba Cyclotron Report No. 72-01.

[23] See AIP document No. PAPS PRVCA-22-2287-89 for the 89 page Supplement to Proton-Proton Bremsstrahlung at 42 MeV: Measurement of Cross Sections and Comparison with a Theoretical Calculation. Order by PAPS number and journal reference from American Institute of Physics, Physics Auxiliary Publication Service, 335 East 45th Street, New York, N. Y. 10017. The price is $1.50 for microfiche, or $13.85 for photocopies. Airmail additional. Make checks payable to the American Institute of Physics.

[24] Hydrogen gas at atmospheric pressure was used as a target. In Exp. I, the entire scattering chamber was filled with commercially pure gas (impurities ~500 ppm). Fifty micron thick Mylar foils, positioned about twice as far from the beam as those indicated in Fig. 1, were used to filter out beam-produced δ rays (cf. Sec. 5.5 in P1). In Exp. II, the target gas was contained in a long, narrow, air-tight gas cell whose sides were also constructed of 50 μm Mylar. After an initial flushing period of 10–20 h, the gas cell was filled with ultra high purity hydrogen (impurities $\lesssim$10 ppm) and a flow rate of several milliliters per second was main-

tained. The remaining part of the scattering chamber was filled with commercially pure hydrogen. The overall purity of the target gas was not precisely known because of contamination in the gas flow system. Estimates based on studies of the data indicated a total contamination of CO_2, O_2, and N_2 of the order of 100 ppm.

[25]The term "resolution" is not defined consistently in the physics literature [see for instance J. Thewlis, *Concise Dictionary of Physics* (Pergamon, Oxford, 1973), and the *International Dictionary of Physics and Electronics* (van Nostrand, Princeton, 1961)]. In this paper, unless otherwise stated, the energy resolution of the final state protons will be defined as $\delta E/E$ with δE expressed as the full width at half maximum (FWHM) of the scintillator pulse-height response curve to beam of mono-energetic protons. For all other variables, the the resolution will be defined as the FWHM of the response curve of the spectrometer to the particular variable in question.

[26]It should be pointed out that this problem is not unique to the experiment reported here. Such a closed loop exists in the evaluation of many experimental results, but its effects are often neglected, either because they are small, or simply because they are overlooked.

[27]M. K. Liou and K. S. Cho, Nucl. Phys. A124, 85 (1969); A145, 369 (1970); A160, 417 (1970). We are very grateful to M. K. Liou for allowing us to use his code for these extensive calculations.

[28]M. K. Liou and M. I. Sobel, Ann. Phys. (N.Y.) 72, 323 (1972).

[29]The original version of the program OWL was written by G. R. Lynch (Berkeley) and modified by J. P. Chandler (Florida State University). The program uses an event generator described by F. James, CERN Report No. 68-15 (1968).

[30]The multiple scattering in the 50 μm Mylar foil was overestimated by a factor of 1.8. This was caused by an inadvertent programming mistake discovered after all the simulated events were produced. Although in some cases the effects of this error were not negligible, it was always possible to make appropriate corrections (see Sec. SVA), thus avoiding the need to repeat the expensive simulation of a large set of ppB events.

[31]Joseph F. Janni, Technical Report No. AFWL-TR-65-150 (1966), distributed by Clearinghouse, Springfield, Virginia.

[32]D. F. Measday and C. Richard-Serre, CERN Report No. 69-17 (1969).

[33]L. G. Greeniaus, J. V. Jovanovich, R. Kerchner, T. W. Millar, P. O'Conner, R. Pogson, W. F. Prickett, C. A. Smith, and K. F. Suen, Manitoba Cyclotron Report No. 75-12, 1975 (unpublished).

[34]Since the energy thresholds for proton detection were relatively high and the electronics which digitized the pulse heights did not have a positive pedestal, it was not known what pulse height corresponded to zero proton energy. As a result, the correction for the nonlinearity of the scintillators at low energies was not applied as it was believed that such a correction would not make the data at low energies any more reliable, while it would, at the same time, complicate the analysis.

[35]D. O. Galde, M. L. Halbert, C. A. Luderman, and A. van der Woude, Phys. Rev. Lett. 25, 1581 (1970).

[36]An experiment using helium gas was done only in conjunction with Exp. I. Since the H_2 target cell was not used in that experiment, there existed some possibility of helium from the wire chambers defusing into the scattering chamber despite the propane filled gap (cf. P1). The test showed that this background was of no importance.

[37]The χ^2 and the missing mass distributions of the air and nitrogen data were sufficiently similar to each other that it did not matter which one was used for the background correction. In practice, the nitrogen data were used since they provided the better statistics.

[38]The overestimation of the angular resolution (see Ref. 30) in the simulated data would have the effect of widening the χ^2 distribution since the difference in the numerator of Eq. (7) would be somewhat increased while the denominator, which was computed on the basis of the experimentally determined resolution, would stay unchanged. As is discussed in T1, the chief contribution to the χ^2 parameter was due to the energy resolution, not the angular resolution. Therefore, it was judged that the widening of the χ^2 distribution due to overestimation of the angular resolution would be small, although not entirely negligible.

[39]U. E. Kruse, J. M. Teem, and N. F. Ramsey, Phys. Rev. 101, 1079 (1956); L. H. Johnston and D. A. Swanson, *ibid.* 111, 212 (1958).

[40]These particular cross sections were used for reasons of convenience and conventionality. The procedures (and programs) are sufficiently general that other sets of cross sections could be also computed.

[41]By combining polar angle bins, the distinction between left and right is lost (see Appendix A). The subscripts used from this point on will be (1) and (2) rather than (L) and (R).

[42]These cross sections have not been corrected for the error in angular resolution. However, any changes in the simulated histograms are sufficiently small that they could not be detected in this figure. All numerical results presented in this paper and the Supplement have been corrected for this effect.

[43]F. Sannes, J. Trischuk, and D. G. Stairs, Nucl. Phys. A146, 438 (1970).

[44]A. Willis, V. Comparat, R. Frascaria, N. Marty, M. Morlet, and N. Willis, Phys. Rev. Lett. 28, 1063 (1972).

[45]It was impossible to avoid using a theoretical model in the simulation of this experiment. As explained in Sec. IV, all events were weighted according to a certain theoretical calculation which was based on one particular model. Setting all of the weights equal to one is equivalent to using just another theoretical (phase space) model.

[46]H. Fearing, *Nucleon-Nucleon Interactions*, *Proceedings of the Second International Conference on Nuclear-Nuclear Interactions, Vancouver, 1977*, edited by H. Fearing, D. Measday, and A. Strathdee (AIP, New York, 1978), p. 506.

[47]This differs from the value of 0.55 ± 0.5 quoted in L3 because of the correction for the overestimation in the multiple scattering (see (Ref. 30).

[48]Note that, in Fig. 28, an *average* value for the square of the matrix element is plotted. This is a good approximation to the matrix element at a given point only

if the matrix element itself is fairly constant over the range of integration. How much this mathematical approximation distorts the shapes of curves in Fig. 28 is hard to say without more detailed calculations, but the approximate independence of the $d\sigma/d\psi_{\gamma'}$ cross sections as a function of θ'_S and θ'_D suggests that these distortions should not be serious.

[49]It is generally believed that the corrections which have not been included in the calculation are not of sufficient magnitude to bring the calculations into agreement with the experimental data.